Journal Pre-proof

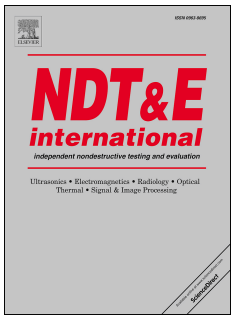

Comparative study of ultrasonic techniques for reconstructing the multilayer structure of composites

Xiaoyu Yang, Erik Verboven, Bing-feng Ju, Mathias Kersemans

PII: S0963-8695(21)00059-1

DOI: https://doi.org/10.1016/j.ndteint.2021.102460

Reference: JNDT 102460

To appear in: *NDT and E International*

Received Date: 18 December 2020

Revised Date: 11 April 2021

Accepted Date: 15 April 2021

Please cite this article as: Yang X, Verboven E, Ju B-f, Kersemans M, Comparative study of ultrasonic techniques for reconstructing the multilayer structure of composites, *NDT and E International*, https://doi.org/10.1016/j.ndteint.2021.102460.

Xiaoyu Yang: Methodology, Software. Validation, Formal analysis, Investigation, Data Curation, Writing - Original Draft, Visualization.

Erik Verboven: Software, Resources, Validation, Investigation.

Bing-feng Ju: Supervision, Project administration, Funding acquisition.

Mathias Kersemans: Conceptualization, Resources, Writing - Review & Editing, Visualization, Supervision, Project administration, Funding acquisition.

Comparative study of ultrasonic techniques for reconstructing the multilayer structure of composites

Xiaoyu Yang[a,b,*,1], Erik Verboven[a], Bing-feng Ju[b] and Mathias Kersemans[a,*]

[a]Mechanics of Materials and Structures (UGent-MMS), Ghent University, Ghent, Belgium
[b]The State Key Laboratory of Fluid Power Transmission and Control, Zhejiang University, Hangzhou, People's Republic of China

ARTICLE INFO

Keywords:
ultrasonics testing
comparative study
deconvolution technique
analytic-signal
multilayer composite
interply track

ABSTRACT

The multilayer structure of fiber-reinforced polymers may be extracted by ultrasonic pulse-echo inspection. Depending on the employed ultrasonic frequency and subsequent processing methodology, different depth resolution and dynamic depth range can be achieved. This study compares the performance of different ultrasonic pulse-echo approaches for extracting the ply-by-ply structure of multilayered composites. The following methodologies are studied: Method 1: 50 MHz, 15 MHz, and 5 MHz ultrasound with low-pass filtering using analysis of the instantaneous amplitude, Method 2: 15 MHz ultrasound with Wiener deconvolution (and AR spectral extrapolation) using analysis of the instantaneous amplitude, and Method 3: 5 MHz ultrasound with low-pass or log-Gabor filtering using analysis of the instantaneous phase. In the simulation study, the performance of the various techniques are investigated on synthetic data representative for a 24-ply carbon fiber reinforced polymer. The robustness of the techniques is evaluated for different signal-to-noise ratios. The various techniques are further investigated on experimental data of a 24-ply cross-ply carbon fiber reinforced polymer. The ply-by-ply structure is extracted and presented in the form of both B-scan and C-scan images. The thickness of each ply is estimated for quantitative analysis. The obtained results indicate that the 5 MHz ultrasound coupled to analytic-signal analysis with log-Gabor filter shows the best performance for reconstructing the multilayer structure of the studied composites.

1. Introduction

Carbon and glass fiber-reinforced polymers (CFRP and GFRP) are widely used in contemporary applications, including space and aviation, automotive, and maritime [1, 2] because of their high specific stiffness (strength) and good corrosion resistance amongst others [3, 4, 5]. To ensure the quality and structural integrity of composite materials, non-destructive testing (NDT) methods can be used [6]. NDT methods play a critical role in the evaluation and maintenance of composite materials. A wide variety of NDT techniques has been built on different principles [7, 8], including x-ray computed tomography [9], terahertz testing [10, 11], infrared thermography [12, 13], shearography [14], eddy current testing [15, 16], ultrasonic testing (UT) [17, 18, 19], etc.

Among the various NDT techniques, UT has been most commonly used for the inspection of multilayer composites [20, 21, 22]. A major advantage of using UT is that it is highly sensitive to the multilayered structure and various damage types commonly found in composites [23]. High-frequency ultrasound can be utilized for the characterization of sub-surface damage with a high spatial and temporal resolution [24, 25, 26]. As the thickness and the number of plies increases, the attenuation of high-frequency ultrasound becomes a concern, especially for high damping fiber-reinforced composites [27]. A recent study reported the inspection of an impacted CFRP laminate using 50 MHz ultrasound and demonstrated a depth probing as deep as 2-2.5 mm [24]. Alternatively, one could lower the ultrasound frequency in order to increase the dynamic depth range, but this is at the expense of the depth resolution. Therefore, researchers have employed various signal processing steps to improve the temporal resolution of the ultrasonic response signal [28, 29].

A simple approach concerns the application of a low-pass (LP) filter to reduce the high-frequency noise [30, 31]. Another common signal processing step is the deconvolution technique in order to estimate the impulse response from the recorded signal in the presence of noise. Some studies have been conducted to compare various deconvolution

*Corresponding author
Email: Xiaoyu.Yang@Ugent.be (X. Yang); Mathias.Kersemans@Ugent.be (M. Kersemans)
ORCID(s): 0000-0002-8019-4284 (X. Yang)

techniques and found that Wiener filtering-based techniques yield good results for online applications [32, 33]. However, a major problem with the Wiener filter is that it produces a deconvolved signal with a narrowband spectrum. Naturally, the signal with a narrowband spectrum has a decreased temporal resolution. Therefore, it was proposed to additionally use an autoregressive (AR) spectral extrapolation [34, 35, 36]. In the application of the AR spectral extrapolation, the deconvolved spectrum with a high signal-to-noise ratio (SNR) is modeled as an AR process, which is then used to extrapolate the low SNR part of the signal spectrum. The combination of the Wiener deconvolution and AR spectral extrapolation in the frequency domain improves temporal resolution and SNR further [37]. This method, however, suffers from the fact that the optimized parameters need to be found through trial and error [36, 37]. Further, the Wiener deconvolution is not valid when both the input signal and the system are unknown [38]. Based on the fact that the input signal typically has a sparse distribution, it has been proposed to find a deconvolution filter whose output distribution is as sparse as possible [39, 40]. Several of such blind deconvolution methods have been developed in order to improve the temporal resolution of the ultrasonic signal [41, 42, 43]. However, note that such blind deconvolution is seldom considered in ultrasonic testing because the impulse response function of an employed ultrasonic system is often well known (or can be easily measured).

Recently, it was proposed to employ an ultrasonic frequency around the ply resonance frequency [44]. Hence, this results in a procedure with a low operating frequency and as such yields a high probing depth in multilayer composites [45, 46]. It was indicated that the instantaneous phase of the analytic-signal becomes locked to the interfaces between plies in certain circumstances. It has been also shown that the phase is more stable than the amplitude for tracking plies, especially when the amplitude is affected by the strong surface echoes [44]. To ensure the accuracy and stability of the phase-derived interply tracking, it is required to fulfill several conditions. The most important condition concerns the use of a pulse with a center frequency that is close to the fundamental ply-resonance frequency. Further, an appropriate bandwidth is required to cope with the various thickness. Too narrow bandwidth cannot cope with variations in ply thickness, while a too wide bandwidth might excite a strong second-harmonic ply resonance, resulting in wrong depth estimations [44, 47, 48]. Furthermore, the application of a log-Gabor filter has been presented to make the phase-derived interply tracking more stable and robust [47].

This study compares the performance of the different ultrasonic approaches for extracting the ply-by-ply structure of composites:

Method 1: 50 MHz, 15 MHz, and 5 MHz ultrasound with LP filtering, using analysis of the instantaneous amplitude,
Method 2: 15 MHz ultrasound with Wiener deconvolution (and AR spectral extrapolation), using analysis of the instantaneous amplitude,
Method 3: 5 MHz ultrasound with LP or log-Gabor filtering, using analysis of the instantaneous phase.

Note that the 5 MHz is a frequency which is commonly used in industry for inspections of aerospace components. Hence, Method 3 can be directly transferred to such an inspection environment without having to change any hardware, or having to scan the parts multiple times.

This paper is organized as follows. Section 2 describes the theoretical framework of the signal processing techniques, including the LP filtering, the deconvolution technique and the analytic-signal technique. Sections 3.1 and 3.2 introduce the analytical model and the used parameters in the simulation. The quantitative evaluation metrics are proposed and described in section 3.3. Sections 3.4 and 3.5 investigate the performance of the different techniques for the synthetic data with different SNR. The experimental results are discussed in section 4. Finally, section 5 presents the conclusions.

2. Background

Finite impulse response (FIR) filters are widely used for LP filtering due to their inherent stability when implemented in non-recursive form and simple extensibility to multi-rate cases. In this study, a FIR LP filter is applied as a pre-processing step to the recorded signals in order to reduce noise features [31]. The cutoff frequency of the FIR LP filter is twice the center frequency of the employed ultrasonic pulse. The transition band steepness is 0.8 and the stopband attenuation is 60 dB.

2.1. Wiener deconvolution with spectral extrapolation

In a linear time-invariant (LTI) system, the response signal $y(t)$ can be modeled as the convolution of the input signal $h(t)$ with the reflection sequence of the specimen $x(t)$, plus the addition of noise $n(t)$ (see Fig. 1):

$$y(t) = x(t) * h(t) + n(t), \tag{1}$$

where $*$ denotes the convolution operator. Eq. (1) can be expressed in the frequency domain as follows:

$$Y(\omega) = X(\omega)H(\omega) + N(\omega), \tag{2}$$

where $Y(\omega)$, $X(\omega)$, $H(\omega)$, and $N(\omega)$ represent the Fourier transforms of $y(t)$, $x(t)$, $h(t)$, and $n(t)$ respectively.

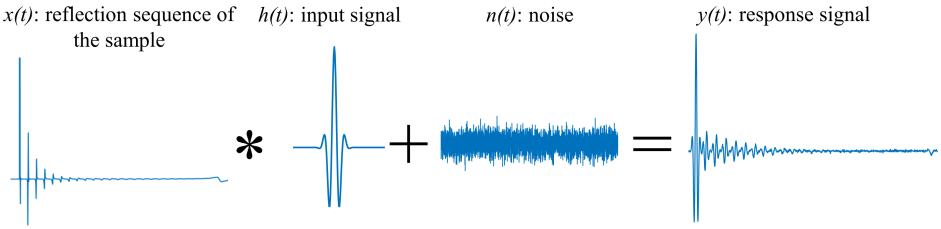

Figure 1: The response signal $y(t)$ from the LTI testing system as the convolution of the input signal $h(t)$ with the reflection sequence of the 24-layer structure $x(t)$ plus the addition of noise $n(t)$. The input signal $h(t)$ has a center frequency of 15 MHz and a fractional bandwidth (-6 dB) of 0.8. The scaling of these waveforms is different both in horizontal (time) and vertical (amplitude) directions.

Considering that $y(t)$ is measured and $h(t)$ is known, a deconvolution procedure can be performed to obtain the deconvolved signal $x_e(t)$ in the presence of noise $n(t)$. To reduce the impact of noise or measurement error, a Wiener filtering in the frequency domain can be applied. A common approach of the Wiener deconvolution can be formulated as [33]

$$X_e(\omega) = \frac{Y(\omega)H^*(\omega)}{|H(\omega)|^2 + Q^2}, \tag{3}$$

where $X_e(\omega)$ represents the Fourier transforms of $x_e(t)$ and Q is the noise desensitizing factor. A commonly recommended value for Q^2 is applied in this study [49, 33]:

$$Q^2 = 10^{-2}|H(\omega)|^2_{\max}, \tag{4}$$

where $|H(\omega)|_{\max}$ is the maximum amplitude of $|H(\omega)|$. The final stage is to employ the inverse Fourier transform to obtain the deconvolved signal in the time domain:

$$x_e(t) = IFT(X_e(\omega)), \tag{5}$$

where $IFT(\bullet)$ denotes the inverse Fourier transform.

To improve the temporal resolution further, AR spectral extrapolation can be applied to the reflection spectrum $X_e(\omega)$ obtained by Wiener filtering. First, a certain bandwidth of the measured reflection spectrum with a high SNR should be selected, whose lower and upper bounds are f_1 and f_2 respectively. The maximum-entropy algorithm of Burg [50] is then used to calculate the AR coefficients from the selected frequency window. Based on the high SNR reflection spectrum, the lower and upper parts of the reflection spectrum are extrapolated as follows:

$$\hat{X}_e(m) = -\sum_{k=1}^{p} a_k X_e(m+k) \quad m = 1, 2, \ldots, \frac{Nf_1}{f_s} - 1, \tag{6}$$

$$\hat{X}_e(n) = -\sum_{k=1}^{p} a_k^* X_e(n-k) \quad n = \frac{Nf_2}{f_s} + 1, \ldots, \frac{N}{2}, \tag{7}$$

where $\hat{X}_e(m)$ and $\hat{X}_e(n)$ are the lower and upper parts of the extrapolated spectrum respectively, N is the sampling points, f_s is the sampling rate, a_k and a_k^* are the AR coefficients and their complex conjugates, respectively, and p is the order of the AR model.

It has been proposed that the extrapolated signals obtained from different frequency windows could improve the robustness of this technique [36]. Hence, the extrapolated spectra from various frequency windows are averaged prior

to performing the inverse Fourier transform for converting the signal into the time domain. The 3 dB to 10 dB drop frequency windows, which are recommended in literature [36], are applied. Following the selection of the frequency window, the following equation is used to select the optimal order p_{opt} for performing the AR spectral extrapolation (with Burg as the fitting method) [51]:

$$p_{opt} = 0.014SNR + 0.21, \tag{8}$$

where SNR is expressed in decibel. Finally, the inverse Fourier transform can be employed on the extrapolated spectrum to obtain the extrapolated signal in the time domain:

$$\hat{x}_e(t) = IFT(\hat{X}_e(\omega)). \tag{9}$$

2.2. Analytic-signal with log-Gabor filter

The analytic-signal $s_a(t)$ represents a signal in its complex form, which is composed of a real part $s(t)$ (see Fig. 2a), and an imaginary part $g(t)$ as follows:

$$s_a(t) = s(t) + ig(t). \tag{10}$$

The imaginary part $g(t)$ is derived from the real part $s(t)$ by the Hilbert transform:

$$g(t) = \int_{-\infty}^{+\infty} \frac{s(\tau)}{\pi(t-\tau)} d\tau. \tag{11}$$

The complex-valued analytic-signal can be represented by its magnitude and phase (see Fig. 2b). The mathematical form also reads as follows:

$$s_a(t) = A_{inst}(t)e^{i\phi_{inst}(t)}, \tag{12}$$

where $A_{inst}(t) = \sqrt{s^2(t) + g^2(t)}$ and $\phi_{inst}(t) = \arctan\frac{g(t)}{s(t)}$ are the instantaneous amplitude and instantaneous phase, respectively (see Figs. 2c and 2d). The instantaneous frequency $f_{inst}(t)$ is then obtained from the time-derivative of the instantaneous phase $\phi_{inst}(t)$:

$$f_{inst}(t) = \frac{1}{2\pi}\frac{d\phi_{inst}(t)}{dt}. \tag{13}$$

The relationship between a signal and its analytic-signal can be represented in the frequency domain as follows [52]:

$$F_a(\omega) = (1 + sgn(\omega))F(\omega), \tag{14}$$

where $F_a(\omega)$ and $F(\omega)$ are the Fourier spectrum of $s_a(t)$ and $s(t)$ respectively, ω is the angular frequency, and $sgn(\bullet)$ denotes the sign function.

The instantaneous amplitude and instantaneous phase can be used to derive the positions of the resin-rich interplies in a composite laminate, on the condition that the center frequency of the ultrasonic input signal approximately corresponds to the fundamental ply-resonance frequency [44]. The instantaneous amplitude is analyzed to derive the time-of-flight (TOF) of the front- and back-wall echoes. The instantaneous phases of the reflections from the resin-rich interplies appear to be close to $\phi_0 - \frac{\pi}{2}$, where ϕ_0 is the instantaneous phase of the input pulse. And the peaks of instantaneous amplitude can also be used to estimate the locations for the resin-rich interplies. The log-Gabor filter [53] decomposes the analytic-signal in different appropriate scales, and as such provides better estimates for the instantaneous phase and instantaneous frequency [47, 54]. The log-Gabor filter is defined in the frequency domain as follows:

$$G(\omega) = \exp\frac{-(\log\frac{|\omega|}{\omega_0})^2}{2(\log\sigma_0)^2}, \tag{15}$$

where ω_0 is the angular center frequency of the passband, σ_0 is the parameter governing the bandwidth of the passband. The log-Gabor filtered analytic-signal in the frequency domain $\tilde{F}_a(\omega)$ can be obtained by

$$\tilde{F}_a(\omega) = G(\omega)F_a(\omega). \tag{16}$$

Its time-domain representation $\tilde{s}_a(t)$ is then obtained by application of the inverse Fourier transform:

$$\tilde{s}_a(t) = IFT(\tilde{F}_a(\omega)). \tag{17}$$

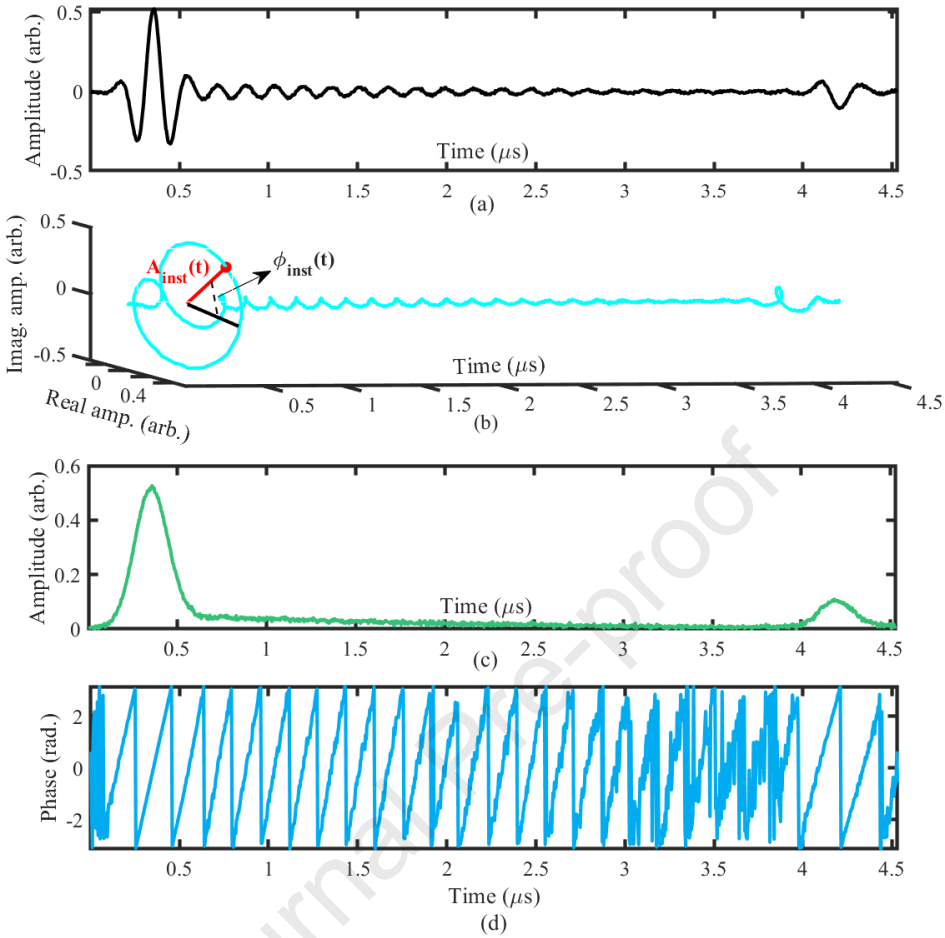

Figure 2: (a) The recorded signal, (b) the analytic-signal in 3-dimensional representation, (c) the instantaneous amplitude, and (d) the instantaneous phase.

3. Simulation study

3.1. Analytical model

The analytical model is implemented in MATLAB. Firstly, the reflection spectrum of the structure is calculated. Secondly, the frequency response is obtained by the multiplication of the Fourier representation of the input signal and the reflection spectrum. Finally, the time-domain reflected signal is obtained and the noise is added. The multilayered structure of a composite laminate immersed in water is illustrated in Fig. 3. The simulated structure consists of 25 interplies (including the front and back surfaces) and 24 plies. Prior to obtaining the complex reflection spectrum of the structure, the acoustic impedance of the n-layered structure is calculated by the recursive method as follows [55]:

$$Z_{\lambda}^{(n)}(\omega) = Z_n \frac{Z_{\lambda}^{(n-1)}(\omega)(e^{2d_n(ik_{zn}-\omega\alpha_n)}+1) - Z_n(e^{2d_n(ik_{zn}-\omega\alpha_n)}-1)}{Z_n(e^{2d_n(ik_{zn}-\omega\alpha_n)}+1) - Z_{\lambda}^{(n-1)}(\omega)(e^{2d_n(ik_{zn}-\omega\alpha_n)}-1)} \quad n \geq 1, \tag{18}$$

where $Z_{\lambda}^{(n)}$ is the total acoustic impedance of the n-layered structure, $Z_n = \rho_n c_{Ln}$ is the acoustic impedance of the nth layer, $k_{zn} = \omega/c_{Ln}$ is the wavenumber in the thickness direction of the nth layer, α_n, d_n, ρ_n, and c_{Ln} are the attenuation, thickness, density, and longitudinal wave velocity of the nth layer respectively. The initial condition is set as $Z_{\lambda}^{(0)} = Z_0$,

which denotes the acoustic impedance of the infinite medium below. The complex reflection spectrum is then obtained as follows:

$$X_s(\omega) = \frac{Z_\lambda^n(\omega) - Z_{n+1}}{Z_\lambda^n(\omega) + Z_{n+1}}, \tag{19}$$

where Z_{n+1} denotes the acoustic impedance of the infinite media above. The reflected signal $y_s^0(t)$ is then obtained as follows:

$$y_s^0(t) = IFT(X_s(\omega)H_s(\omega)), \tag{20}$$

where $H_s(\omega)$ is the complex Fourier representation of the input signal $h_s(t)$. White Gaussian noise $n_s(t)$ is considered which has uniform power over the considered frequency band and normal distribution in the time domain with zero mean value. The reflected signal $y_s(t)$ finally becomes:

$$y_s(t) = y_s^0(t) + n_s(t). \tag{21}$$

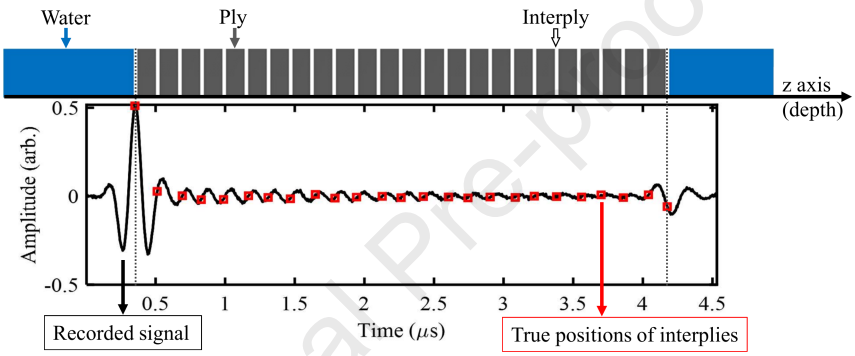

Figure 3: The schematic of the multilayered structure and the signal response.

3.2. Simulation parameters

The interply is considered as a thin epoxy layer of 10 μm with a density of 1270 kg/m^3. The ply is considered as a mixture of unidirectional fibers and epoxy matrix with a fiber volume fraction of 60% [56]. When defining the effective mass density of the ply, the rule of mixture is applied, assuming a density of the carbon fibers of 1800 kg/m^3. The stiffness matrix for each ply is calculated by the Chamis model [57] from the properties of carbon fiber [58] and epoxy matrix. The longitudinal wave velocity propagating in the thickness direction is then calculated from the stiffness matrix. To fully evaluate the performance of the various ultrasonic techniques, a 24-layer laminate with various ply thicknesses is simulated. It is important to consider possible variations in the ply thickness because CFRP plies do not have necessarily a uniform thickness. This variation is mainly introduced during the manufacturing cycle due to resin flow effects before the polymerisation in the autoclave [59, 60]. Hence, a combination of 3 different ply thickness sequences is applied for the simulated data as follows: (i) a uniform ply thickness of 220 μm, (ii) a ply thickness sequence of $[220\mu m/210\mu m/230\mu m]_8$, and (iii) a ply thickness sequence of $[220\mu m/230\mu m/210\mu m]_8$. It is worth noting that the varying ply thickness is more challenging for the analysis of the instantaneous phase due to the fact that it requires a center frequency close to the ply-resonance frequency. Table 1 displays the used properties of the interply, the ply, and the immersion liquid.

The input signal is modeled as a cosine modulated by a Gaussian function:

$$h_s(t) = \exp\left(\frac{t^2 W^2 F_c^2 \pi^2}{4\ln(0.5)}\right)\cos(2\pi F_c t), \tag{22}$$

where t is the time vector, W is the -6 dB fractional bandwidth of the pulse, F_c is the center frequency (see Fig. 4). A nominal SNR of 25 dB is used, which can be considered representative for actual experiments. A sampling rate of 250 MS/s is adopted. Table 2 provides the parameters concerning the input signal and data acquisition.

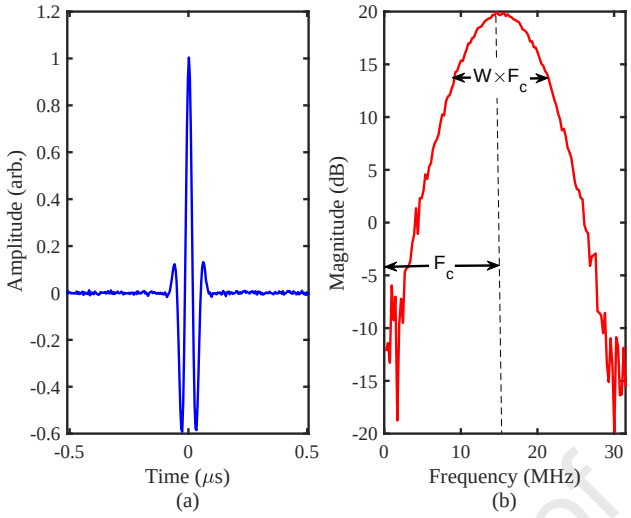

Figure 4: (a) The input signal with a center frequency of 15 MHz and the nominal SNR of 25 dB and (b) its corresponding frequency spectrum.

Table 1
The properties of the interply, the ply, and the immersion liquid.

Name	Materials	Density (kg/m^3)	Thickness (μm)	Wave velocity (m/s)	Attenuation (dB/mm/MHz)
Interply	epoxy	1270 [61]	10	2499 [58]	0.15 [61]
Ply	Mixture of unidirectional fibers and epoxy matrix with a fiber volume fraction of 60%	1588	(i) 220 (ii) $[220/210/230]_8$ (iii) $[220/230/210]_8$	2906	0.1 [62]
Immersion liquid	water	1000		1480	

Table 2
Parameters of the input signal and data acquisition.

Center Frequency (MHz)	-6 dB fractional bandwidth	Bonding media	Nominal SNR (dB)	Sampling rate (MS/s)
5, 15, 50	0.8	water	25	250

3.3. Evaluation metrics

This study uses a quantitative approach to investigate the performance of different ultrasonic techniques. The LP filtered signal is obtained by the application of the LP filter to the original signal $y_s(t)$ in Eq. (21), and the TOF of the interplies is estimated from the local maxima in the instantaneous amplitude (see Fig. 5a). The deconvolved signal equals $x_e(t)$ in Eq. (5) (or $\hat{x}_e(t)$ in Eq. (9) when considering spectral extrapolation), and the TOF of the interplies is estimated from the local maxima in the instantaneous amplitude (see Fig. 5a). The analytic-signal equals $s(t)$ in Eq. (10) (or $\tilde{s}_a(t)$ in Eq. (17) when considering a log-Gabor filter), and the TOF of the interplies is estimated from the instantaneous phase (see Fig. 5b). The detailed procedure for estimating the TOF of the interplies is given in the flowcharts in Fig. 6.

Once the TOF of the interplies are estimated, the error ε^i is calculated as (see also Fig. 5):

$$\varepsilon^i = TOF^i_{est} - TOF^i_{true}, \tag{23}$$

where TOF^i_{est} and TOF^i_{true} are the estimated and the true TOF of the ith interply respectively. The measurement error

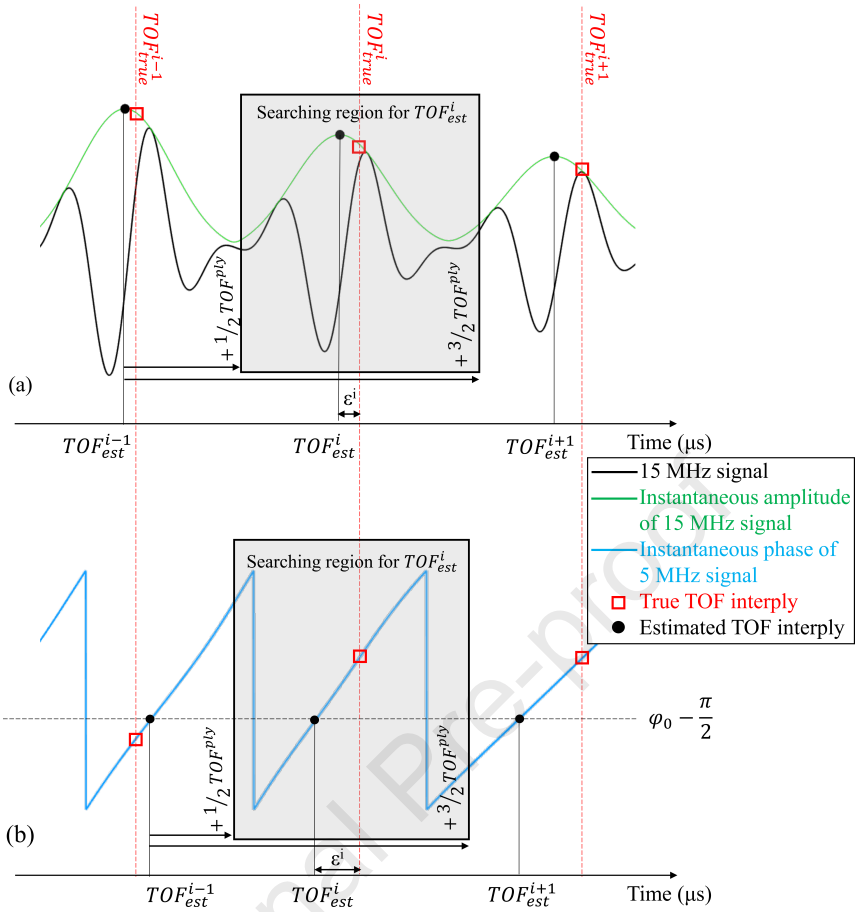

Figure 5: Schematic illustration of TOF estimation of the interplies based on (a) the instantaneous amplitude of a 15 MHz signal, and (b) the instantaneous phase of a 5 MHz signal. Note: the graphs are only for illustration purposes, and do not correspond to real data.

E^i of each interply i is calculated as follows:

$$E^i = \frac{\varepsilon^i}{TOF^{ply}} \times 100[\%], \tag{24}$$

where TOF^{ply} is the true TOF of a single-ply. For each ply thickness sequence, each simulation procedure is repeated 100 times. The statistical information is extracted from the 300 runs in total. The mean measurement errors (ME^i) and the standard deviations of the measurement errors ($STDE^i$) are evaluated:

$$ME^i = \frac{\sum_{j=1}^{N} E^i_j}{N}, \tag{25}$$

$$STDE^i = \sqrt{\frac{\sum_{j=1}^{N}(E^i_j - \overline{E^i_j})^2}{N}}, \tag{26}$$

where E^i_j is the measurement errors E^i in the jth repeat, and N is the number of signals considered.

In general, the ME^i and the $STDE^i$ indicate the accuracy and the robustness for estimating the TOF of the ith interply, respectively. Therefore, the error bars representing the ME^i and the $STDE^i$ can provide a comprehensive evaluation of the performance visually. However, the SNR of the signal is occasionally not high enough for properly distinguishing the interply reflections. In case the TOF^i_{est} is randomly distributed (over the 300 runs) in the searching region and the true TOF of the interply is located in the middle of the searching region, this would result in an ME^i of 0% and an $STDE^i$ of 28.9%, which means the sensitivity to the variations of the ply thickness is completely lost.

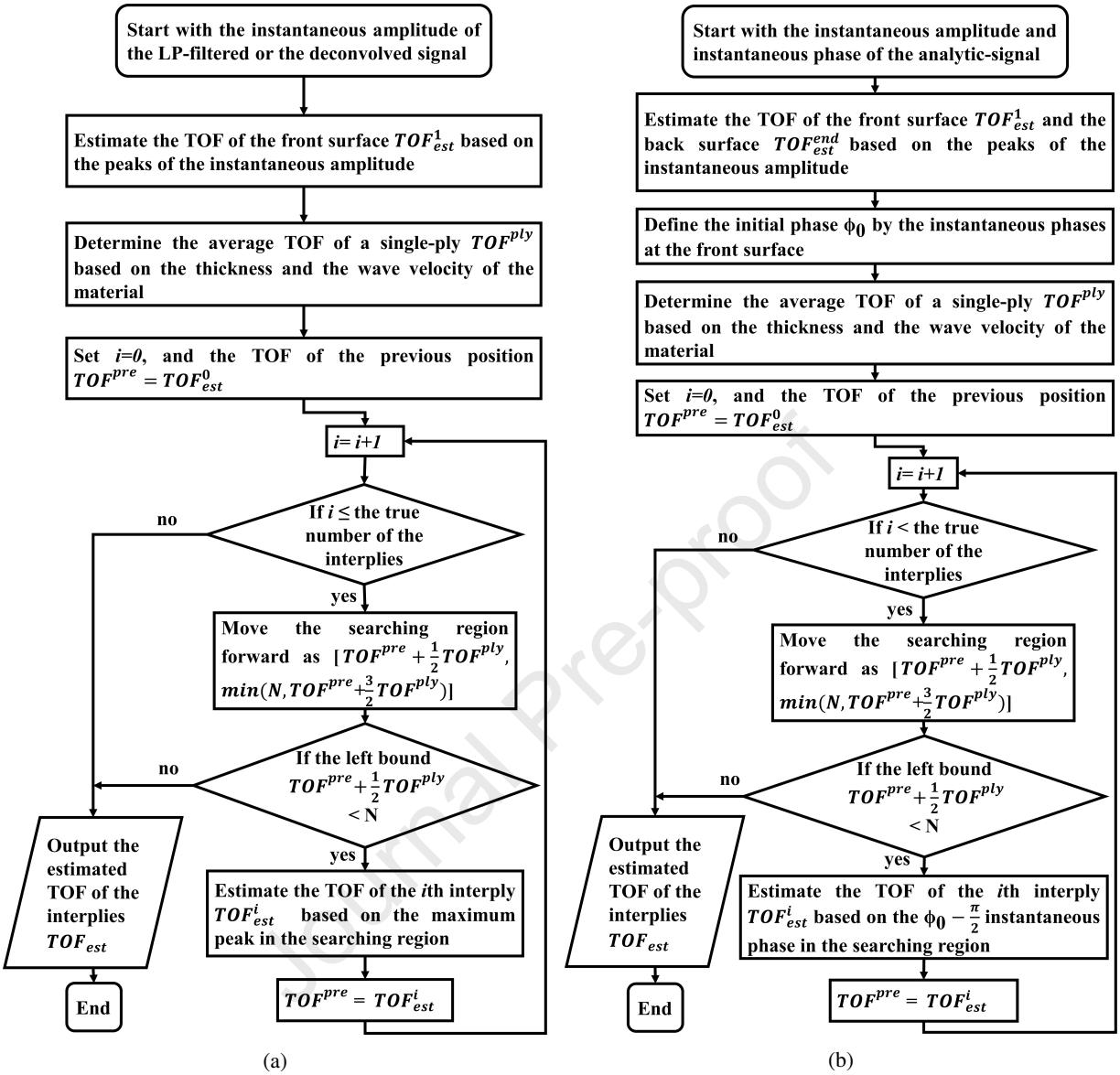

Figure 6: Flowcharts for estimating the TOF of the interplies by using (a) the instantaneous amplitude (Methods 1 and 2) and (b) the instantaneous phase (Method 3).

Hence, to determine whether the interply reflections are distinguishable, a threshold of the $STDE^i$ is set at 22%. The lower the $STDE^i$, the better the interply reflections are distinguishable.

3.4. Results

3.4.1. Low-pass filtered signal using instantaneous amplitude (50 MHz; 15 MHz; 5 MHz)

The resolution and dynamic depth range of an ultrasonic signal are directly linked to its frequency. Fig. 7 displays the simulation results for an input signal with center frequencies of 5 MHz, 15 MHz, and 50 MHz, respectively. The instantaneous amplitudes of the response signals have been extracted by Hilbert transform, from which the positions of the interplies are estimated according to the procedure defined in section 3.3. The true TOF of the interplies are indicated with the vertical dashed lines. From Fig. 7, it becomes clear that a higher center frequency produces sharper peaks at the positions of the interplies, but at the same time experiences more severe attenuation. The ME^i and $STDE^i$ of the estimated interplies are presented in Fig. 8. The front-surface and back-surface interplies are indicated

with F and B respectively. The interplies i are indicated by their depth position, starting from $i = 1$ for the first interply until $i = 23$ for the last interply. If the $STDE^i$ becomes larger than 22% (= interply i could not be distinguished in a proper way), the value for interply i is greyed out.

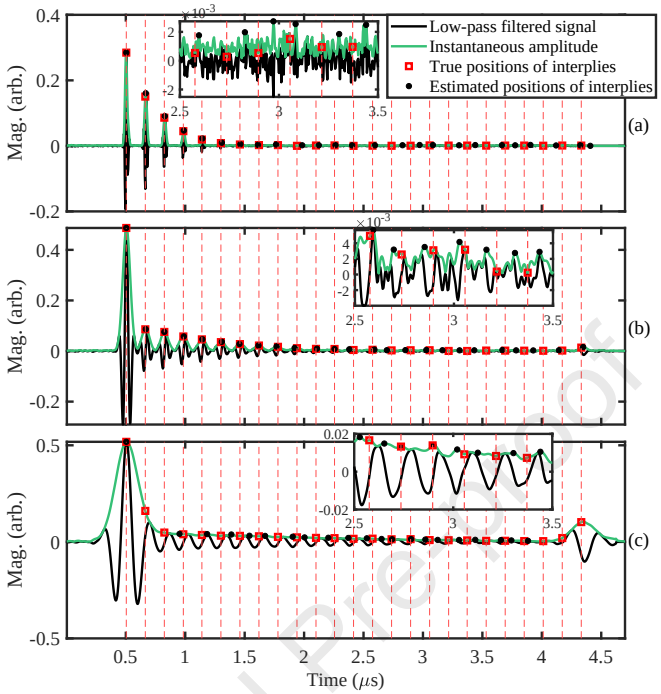

Figure 7: The LP filtered signals with center frequencies of (a) 50 MHz, (b) 15 MHz, and (c) 5 MHz respectively, including the instantaneous amplitude (green trace), and the true and estimated positions of the interplies (red square and black dot respectively).

The 50 MHz LP filtered signal produces sharp and clear peaks for the first 7 interplies, and locates the positions of these interplies in an accurate and robust manner. After the 8th interply, there is a sharp rise in the $STDE^i$. It can also be observed in Fig. 7a that a back-wall echo is not present due to excessive attenuation. Hence, the 50 MHz signal provides high depth resolution in the near-surface plies but becomes impractical due to its low SNR for deeper layers (see also the inset in Fig. 8a).

The 15 MHz LP filtered signal has higher $STDE^i$ for the near-surface plies, but it remains longer stable for deeper layers. The $STDE^i$ remain within 10% for the first 9 interplies. The graph reveals the gradual rise in the $STDE^i$ until it becomes fully unstable for plies deeper than the 14th interply. And an increase in the bias can be seen from the ME^i after the 12th interply. The observed gradual deterioration over depth makes the 15 MHz signal particularly well suited for the deconvolution procedure in order to increase the depth resolution (section 3.4.2).

The 5 MHz ultrasound efficiently penetrates through the whole structure and produces a well-defined back-wall echo. However, the instantaneous amplitude of the 5 MHz LP filtered signal is clearly not valid for extracting the interpliy locations (see Fig. 7c). The amplitude near the surfaces is completely affected by the strong surface echoes. Consequently, no peak of instantaneous amplitude is tracked for the 1st interply (see Fig. 8c). In order to cope with the effects of the front-surface echo on the detection of the 1st interply echo, it is valid to adopt the local minimum of the second derivative of the instantaneous amplitude. Whereas, this procedure is not included in the comparative study since it is non-standard. It can also be seen that the ME^i is very large and $STDE^i$ exceeds the value of 22% instantly. Hence, it may be expected that the application of deconvolution will not provide any significant improvement for the 5 MHz signal. Instead, the 5 MHz signal will be coupled to the analytic-signal analysis, and the instantaneous phase will be used for estimating the positions of the interplies (section 3.4.3).

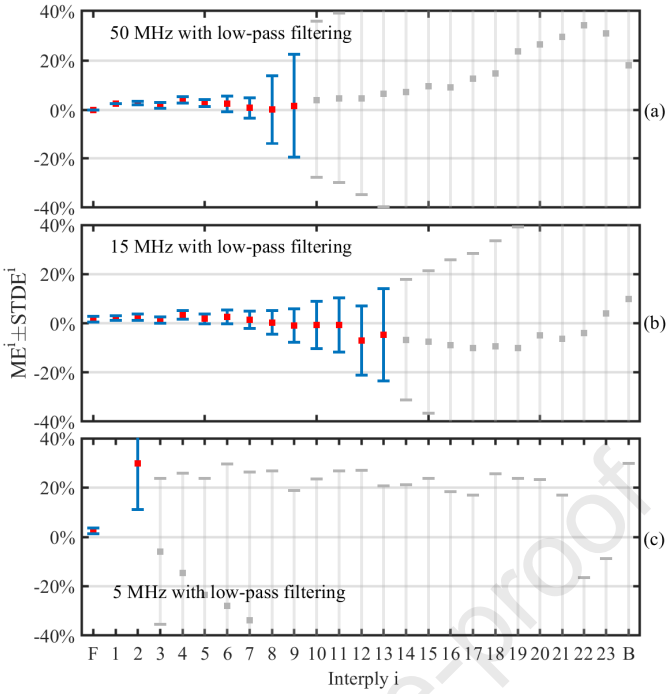

Figure 8: Error bars representing the ME^i and the $STDE^i$ of the estimated interplies from the instantaneous amplitudes of the LP filtered signals with center frequencies of (a) 50 MHz, (b) 15 MHz, and (c) 5 MHz respectively. The data is represented as $ME^i \pm STDE^i$.

3.4.2. Deconvolved signal using instantaneous amplitude (15 MHz)

Based on the response signals (see Figs. 7 and 8), it is anticipated that the application of deconvolution is a practical way to improve the depth resolution for the 15 MHz signal. Fig. 9 displays the deconvolved signal with a center frequency of 15 MHz from Wiener deconvolution and Wiener deconvolution combined with AR spectral extrapolation. The input pulse with the nominal SNR of 25 dB is used as the deconvolution kernel. Table 3 lists the 3 dB to 10 dB drop frequency windows for multiple frequency windows AR spectral extrapolation. The optimal order p_{opt} of the AR process is chosen according to Eq. (8) for each window. The instantaneous amplitudes of the deconvolved signals have been extracted by Hilbert transform, from which the positions of the interplies are estimated according to the previously defined procedure (see section 3.3).

From Fig. 9 it can be seen that the deconvolution techniques improve the temporal resolution and SNR (compared to the 15 MHz LP filtered signal in Fig. 7b). The ME^i and the $STDE^i$ of the estimated interplies from the LP filtered and the deconvolved signals are compared in Fig. 10. Compared to the LP filtered signal, the Wiener deconvolution has a minor effect on the ME^i, but reduces the $STDE^i$ significantly. Hence, this indicates that the extraction of interply locations is more stable and robust. Still, for very deep layers (>17th interply) the $STDE^i$ rapidly converges again to the values above 22%, indicating completely random TOF estimation.

Contrary to the expectation, the deconvolved signal by Wiener filtering with optimized AR spectral extrapolation shows the worst performance of the approaches used in Method 2. This is possibly due to the fact that the AR process is quite sensitive to noise [63]. Further, it has been reported that some spurious spikes could be observed in the deconvolved ultrasonic signal by optimized AR spectral extrapolation [51]. These spurious spikes could be large in amplitude and could become comparable to the actual signal. This is especially valid for the current situation because the reflection signal from the interplies is weak. Hence, the Wiener deconvolution combined with AR spectral extrapolation is not a suitable approach for the here considered case.

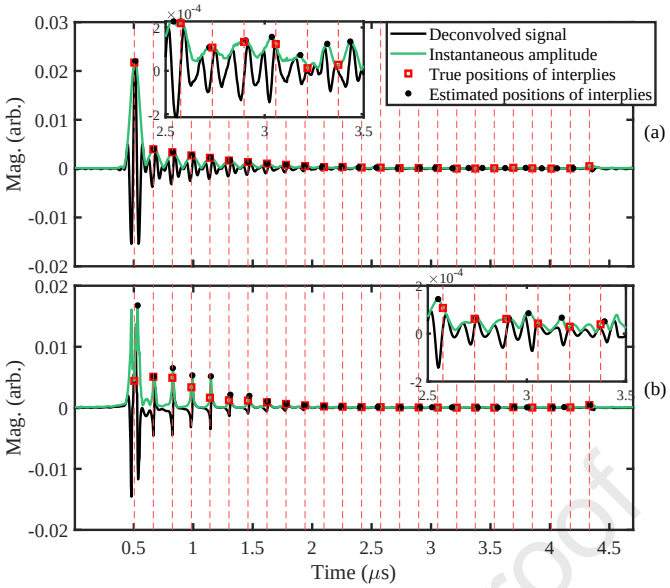

Figure 9: The 15 MHz deconvolved signals by (a) Wiener deconvolution and (b) Wiener deconvolution combined with AR spectral extrapolation respectively, including the instantaneous amplitude (green trace), and the true and estimated positions of the interplies (red square and black dot respectively).

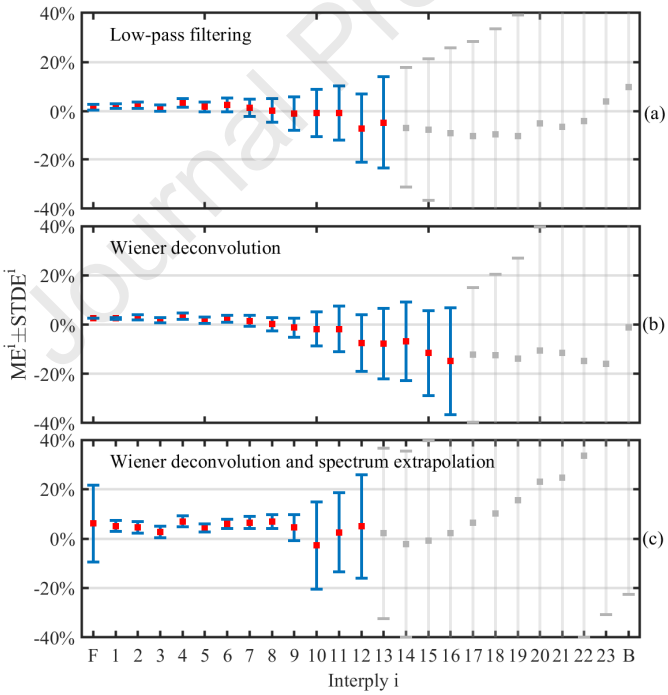

Figure 10: Error bars representing the ME^i and the $STDE^i$ of the estimated interplies from the instantaneous amplitudes of (a) the 15 MHz LP filtered signal, (b) the 15 MHz Wiener deconvolved signal, and (c) the 15 MHz Wiener deconvolved signals combined with AR spectral extrapolation. The data are represented as $ME^i \pm STDE^i$

Table 3
The frequency windows and the optimal orders considered for multiple frequency windows AR spectral extrapolation.

Drop (dB)	Frequency range (MHz)	Data points	p_{opt}
-3	10.8-19.2	88- 158	39
-4	10.1-19.9	83- 163	45
-5	9.5-20.5	78- 168	50
-6	9.0-21.0	74- 172	55
-7	8.5-21.5	70- 176	59
-8	8.1-21.9	66- 180	64
-9	7.7-22.3	63- 183	67
-10	7.3-22.7	59- 186	71

3.4.3. Analytic-signal using instantaneous phase (5 MHz)

From the analysis presented in section 3.4.1, it became clear that the instantaneous amplitude of the 5 MHz LP filtered signal could not be used for estimating the positions of the interplies, except for the front-surface and the back-surface interplies. Considering that the frequency of 5 MHz is close to the ply-resonance frequency, the instantaneous phase could offer an effective way of estimating the positions of the interplies (see section 2.2).

Fig. 11a displays the instantaneous amplitude, instantaneous phase, and instantaneous frequency of the 5 MHz LP filtered analytic-signal. The TOF between the front- and back-wall echoes is approximately 3.8 μs, which indicates a ply-resonance frequency of 6.3 MHz. So 5 MHz is lower than the ply-resonance frequency. However, the instantaneous phase analysis still works here because the bandwidth in the 5 MHz pulse is sufficiently wide in order to excite the 6.3 MHz ply-resonance in an efficient manner. In order to match the input signal better to the ply resonance, a log-Gabor filter is additionally applied for optimal scale selection. The center frequency and σ_0 for the log-Gabor filter are chosen as 6.3 MHz and 0.7, respectively.

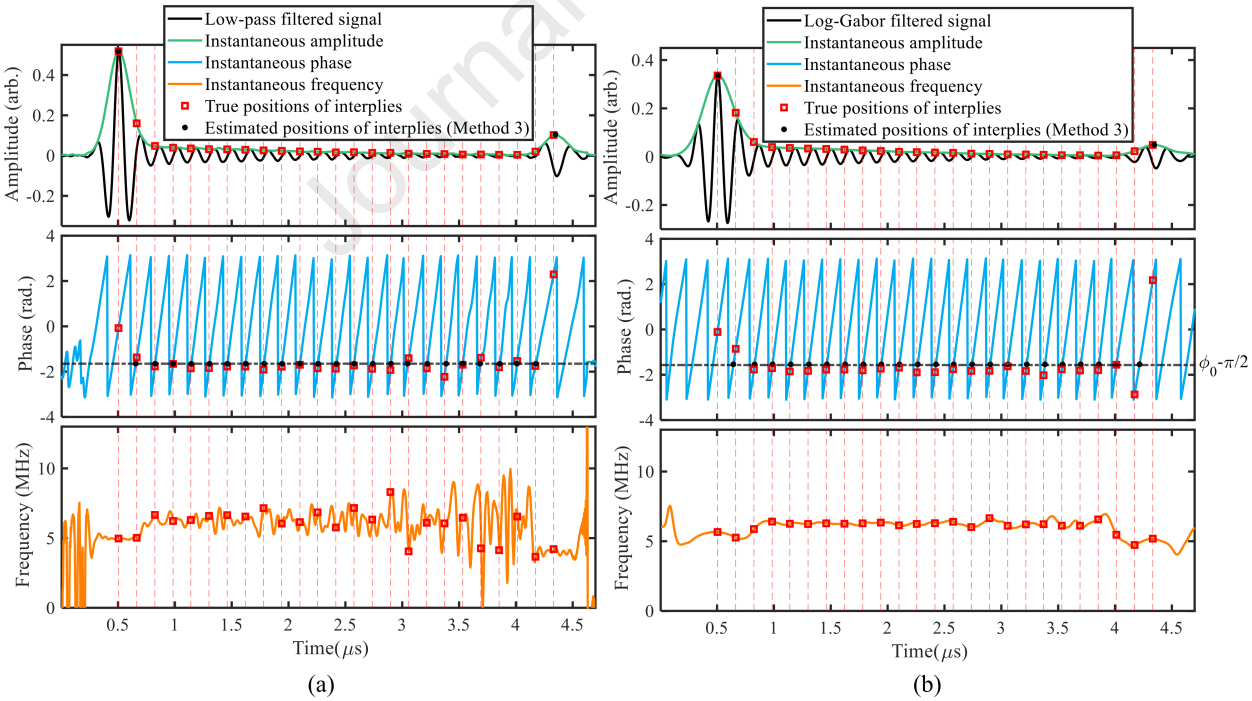

Figure 11: The 5 MHz analytic-signals (a) with LP filtering, and (b) log-Gabor filtering, including the instantaneous amplitude (green trace), the instantaneous phase (blue trace), the instantaneous frequency (orange trace). The true and estimated positions of the interplies are indicated by red squares and black dots respectively.

Fig. 11b displays the instantaneous amplitude, instantaneous phase, and instantaneous frequency of the 5 MHz analytic-signal with the application of the log-Gabor filter. One can readily see the effect of the filter on the quality of the signals, especially on the instantaneous frequency. Compared to the LP filtered analytic-signal in Fig. 11a, the log-Gabor filtered analytic-signal shows a steadier instantaneous frequency around the fundamental ply-resonance frequency in Fig. 11b. The ME^i and the $STDE^i$ obtained from the 5 MHz signals are compared in Fig.12.

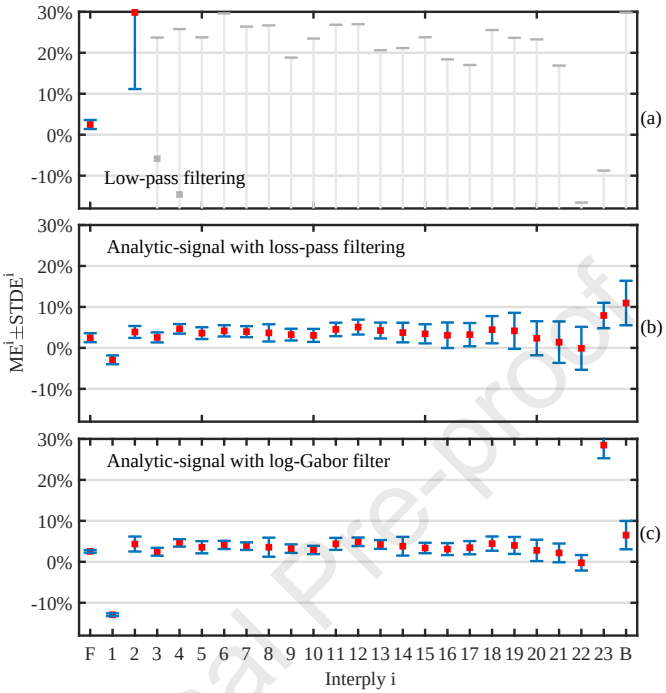

Figure 12: Error bars representing the ME^i and the $STDE^i$ of the estimated interplies from (a) the instantaneous amplitude of the 5 MHz LP filtered signal, and the instantaneous phase of the 5 MHz (b) LP filtered and (c) log-Gabor filtered signals. The data is represented as $ME^i \pm STDE^i$.

While the instantaneous amplitude does not give any indication of the positions of the interplies, the instantaneous phase provides steady results for all interplies. It is worth noting that the $STDE^i$ is significantly improved by the application of the log-Gabor filter. However, the estimated TOF of the interplies near the surfaces shows large ME^i (around -15% for the 1st interply and +28% for the 23rd interply) due to the dominating effect of the front- and back-wall echoes [44]. Compared to the analytic-signal with LP filtering in Fig. 12b, the log-Gabor filter reduces the random errors considerably, but magnifies the ME^i in the 1st and the last plies. The $STDE^i$ steadily increases with depth, but remains below 5% by application of the log-Gabor filter, indicating the high robustness of the TOF estimation. The log-Gabor filter is suggested as a better choice because of its high robustness.

3.5. Comparative analysis for different noise levels

The performance of the various techniques for different noise levels is investigated in this section. The results for 3 SNRs (25 dB, 20 dB and 15 dB) are simulated and analyzed. Fig. 13 compares the ME^i and the $STDE^i$ for the various techniques and noise levels.

From Fig. 13, it is clear that the 50 MHz ultrasound coupled to the LP filtering is not a good approach for extracting the deep interply locations. For the SNR of 15 dB, this method already yields random results from the 7th interply on. On the other hand, it keeps a very high resolution and good stability for the near-surface plies under all the considered noise levels. In a similar way, the 15 MHz ultrasound with Wiener deconvolution becomes more unstable for lower SNR. The $STDE^i$ increase significantly with the SNR, and for the lowest SNR of 15 dB the performance of this approach dropped significantly.

In contrast to previous techniques, the 5 MHz ultrasound coupled to analytic-signal analysis with log-Gabor filter performs very well for all considered noise levels. Further, for the SNR of 25 dB and 20 dB it can be noted that the ME^i

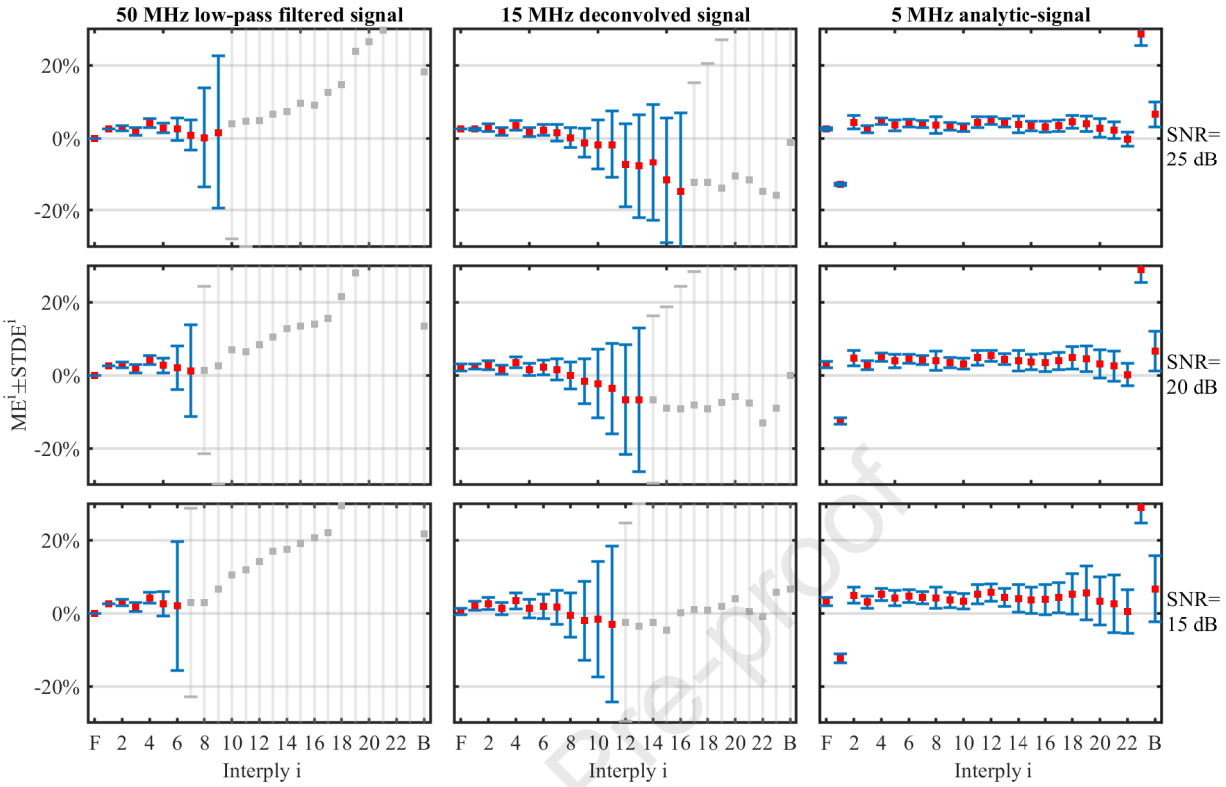

Figure 13: Error bars representing the ME^i and the $STDE^i$ of the estimated interplies from the 50 MHz LP filtered signal (first column), the 15 MHz signal with Wiener deconvolution (second column), and the 5 MHz analytic-signal with log-Gabor filter (third column). Results are obtained for different SNRs: 25 dB (first row), 20 dB (second row), and 15 dB (third row). The data is represented as $ME^i \pm STDE^i$.

of the second and second last interply peaks, while their $STDE^i$ is very small. This indicates a systematic error in the extraction of the location of these two interplies through the instantaneous phase [44, 47]. For the lowest SNR, the ME^i remains quite stable over all interplies, although the $STDE^i$ increases to some extent. The good performance for all considered SNR levels can be attributed to the use of a log-Gabor filter. Indeed, apart from providing an appropriate scale selection, it also suppresses noise features.

4. Experimental study

4.1. Materials and Methods

A CFRP laminate (autoclave manufactured) with dimension 150 mm Œ 100 mm and a thickness of 5.52 mm is studied. It consists of 24 unidirectional plies and has a stacking sequence $[45/0/-45/90]_{3s}$. Each ply is assumed to have a constant and uniform thickness. The inspection procedure takes approximately 10 minutes, such that water diffusion in the inspected composite sample is of little concern [64, 65].

Three different spherically focused broadband immersion transducers (center frequency of 5 MHz, 15 MHz, and 50 MHz) are employed. Table 4 presents the properties of the transducers applied in this experimental study. Reference signals reflected from a thick steel plate are acquired to calculate the SNR and the bandwidth (at -6 dB) of different transducers. The reference signal of the 15 MHz transducer is used as the deconvolution kernel for the Wiener deconvolution. The transducers are excited by an ultrasonic pulser (Tecscan UTPR-CC-50). The exciting pulse is a negative square wave with a pulse width of 30-500 ns (according to the setting), a rise time below 5 ns, and a fall time below 20 ns. The employed settings for the pulser including the voltage, capacity, and damping are also presented in Table 4. To achieve the raster scanning, a 3-axis Cartesian scanner is used which is controlled using a motion controller card (NI PXI-7350). The scanning steps in both x and y directions are 0.5 mm and the scanning area X×Y = 50 mm×50

Table 4
The properties of the employed transducers and the corresponding settings for the pulser

Properties of transducers							Settings for pulser		
Manufacturer	Code	Freq.	Bandwidth (-6 dB)	Elem. d.	Focal l.	SNR	Voltage	Capacity	Damping
GE	H5M	5 MHz	2.43 - 6.61 MHz	6.35 mm	25.4 mm	39.42 dB	120 V	1070 pF	45 Ohm
Olympus	V313	15 MHz	10.84 - 23.08 MHz	6.35 mm	25.4 mm	28.20 dB	120 V	920 pF	78 Ohm
Olympus	V390	50 MHz	26.31 - 61.85 MHz	6.35 mm	12.7 mm	26.84 dB	120 V	450 pF	500 Ohm

mm (100×100 data points) for all transducers. The scanning procedure and excitation/acquisition sequence have been programmed in a custom-made LabVIEW® program. The reflected signals from the CFRP laminate, for the different employed transducers, are displayed in A-scan mode in Fig. 14.

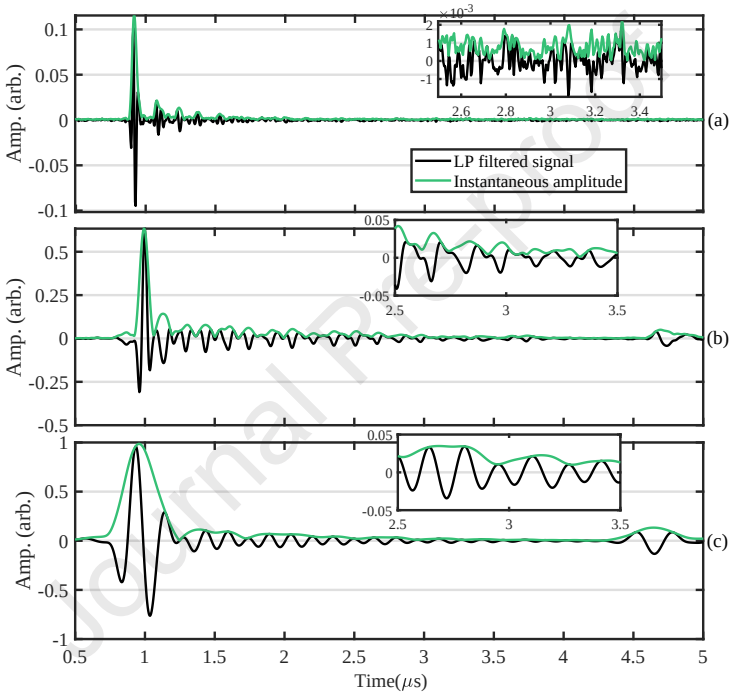

Figure 14: The LP filtered signal, including the instantaneous amplitude (green trace), from the CFRP laminate for different employed transducers with center frequency (a) 50 MHz, (b) 15 MHz, and (c) 5 MHz.

After collecting the data by the raster scanning, the 3D data matrix is sent to Matlab® in order to reconstruct the positions of the interplies using the flow chart presented in section 3.3. According to the instantaneous amplitude of the 5 MHz LP filtered signals, the TOF between the front- and back-wall echo is approximately 3.67 μs, which indicates an approximate ply-resonance frequency of 6.5 MHz. Thus, the center frequency and σ_0 of the log-Gabor filter applied on the 5 MHz signals are chosen as 6.5 MHz and 0.7 respectively.

4.2. Comparison and discussion

Fig. 15 displays the B-scan representation at Y = 25 mm of the instantaneous amplitude from the 50 MHz LP filtered signals, the 15 MHz Wiener deconvolved signals, and the 5 MHz log-Gabor filtered signals. 3 optimal techniques are here applied to estimate positions of the interplies as follows:

Method 1: the 50 MHz LP filtered signal using analysis of the instantaneous amplitude,
Method 2: the 15 MHz Wiener deconvolved signal using analysis of the instantaneous amplitude,
Method 3: the 5 MHz log-Gabor filtered analytic-signal using analysis of the instantaneous phase.

The estimated positions of the interplies and the uniformed-spaced positions of the interplies are superimposed on these B-scan images. The difference in the quality to extract the interply locations can be readily seen in Fig. 15. In order to quantify this, the thicknesses of the plies are estimated from the estimated positions of the interplies in each data point. The mean estimated thickness MT^p and the standard deviations of the estimated thickness $STDT^p$ of the pth ply are calculated as:

$$MT^p = \frac{\sum_{q=1}^{m} T_q^p}{m}, \tag{27}$$

$$STDT^p = \sqrt{\frac{\sum_{q=1}^{m} (T_q^p - \overline{T_q^p})^2}{m}}, \tag{28}$$

where T_q^p is the estimated thickness of the pth ply from the A-scan in the qth data point, and m is the number of the data points in the scanning area (100×100=10000).

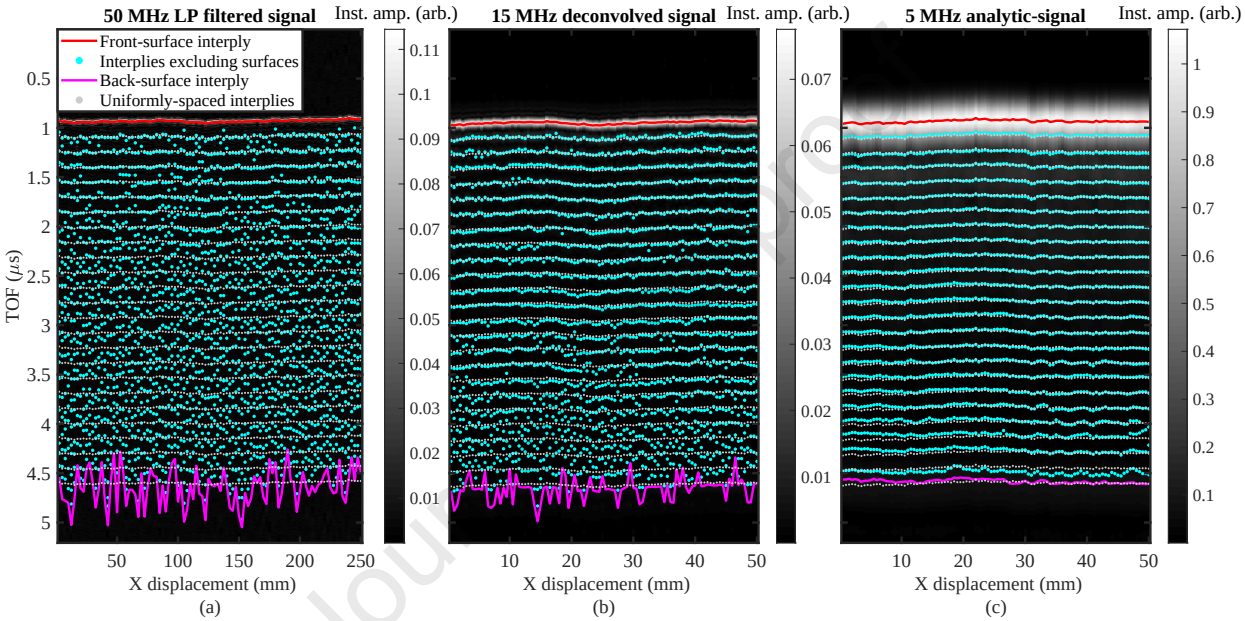

Figure 15: B-scan ultrasound images (at Y = 25 mm) of the instantaneous amplitude from (a) 50 MHz LP filtered signals, (b) 15 MHz signals with Wiener deconvolution, and (c) 5 MHz analytic-signals with log-Gabor filter. Superimposed are the estimated positions of the interplies and the uniformly-spaced positions of the interplies

Note that care has to be taken when interpreting these metrics because they include the variation of the actual thickness in each single ply. Fig. 16 displays the obtained MT^p and $STDT^p$ for the three considered cases. From the total thickness of the sample (5.52 mm), and the true number of plies (24 plies), the expected thickness of a single ply is calculated as 5.52/24 = 0.23 mm (see the dashed line in Fig. 16). This is of course under the assumption that the autoclave manufacturing process yields a uniformly-spaced ply thickness (T^{us}) over depth and over the CFRP sample. Similarly as for the numerical case, if the $STDT^p$ becomes higher than 22% the T^{us}, the extracted results are assumed to be random and are therefore greyed out in the graph.

The 50 MHz signals show a very uniform MT^p over the full depth (see Fig. 16a). However, evaluation of $STDT^p$ tells a different story and indicates the randomness of the estimated ply thickness for deeper plies. This can be also verified in Fig. 15a. Hence, this clearly indicates the poor performance and robustness of this method to resolve the ply structure of the CFRP composite. The 15 MHz signals with Wiener deconvolution provide better probing depth and robustness (see Fig. 15b). Nearly 18 plies can be distinguished, but the $STDT^p$ increases significantly with depth. This can also be verified in Fig. 16b.

The 5 MHz analytic-signals with log-Gabor filter provide the best results and are able to extract all 24 plies in a stable and robust way (see Fig. 16c). This can be also verified in Fig. 15c. However, one of the issues that emerge from these results is that there are large systematic errors in the most shallow and deepest plies. The estimated thicknesses of

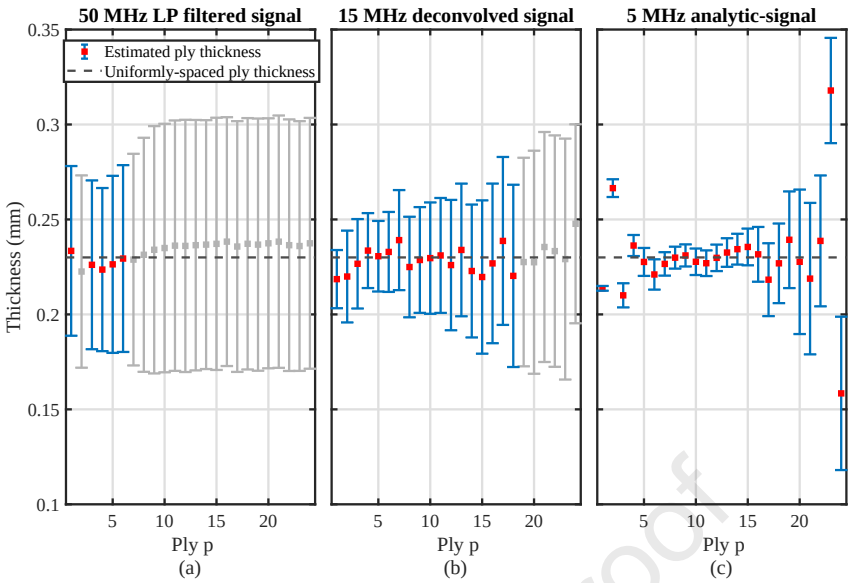

Figure 16: Error bars representing the MT^p and the $STDT^p$ of the plies from (a) 50 MHz LP filtered signals, (b) 15 MHz signals with Wiener deconvolution, and (c) 5 MHz analytic-signals with log-Gabor filter. The data is represented as $MT^p \pm STDT^p$.

those plies show significant deviations from the T^{us} (see Fig. 16c). A similar observation was made in the simulation study (see Fig. 12c), and this systematic deviation has been attributed to the dominating effect of the front- and back-wall echo.

Fig. 17 provides a C-scan representation of the estimated depth of several interplies by considering the three afore-

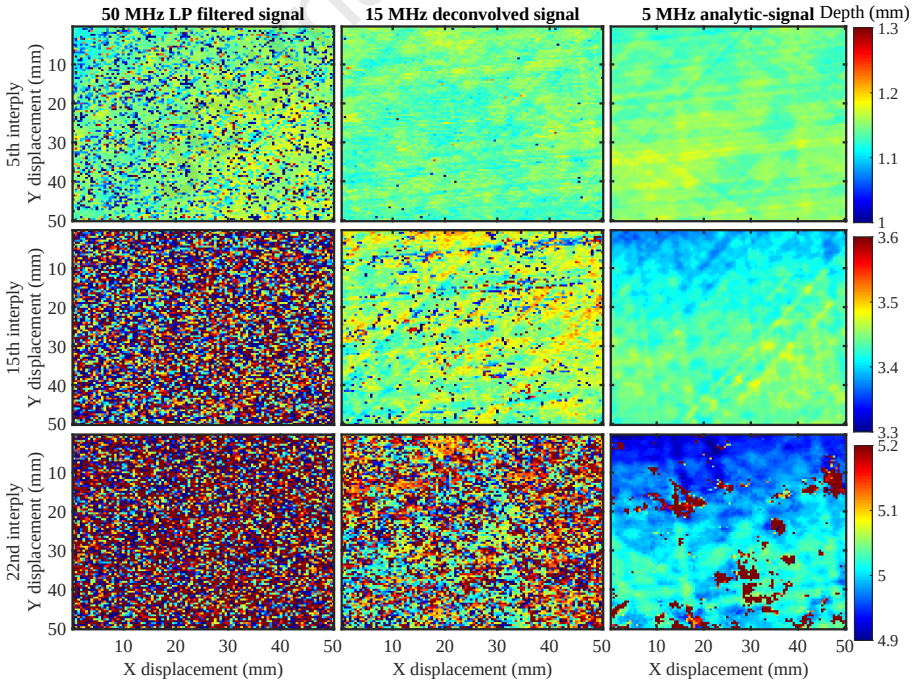

Figure 17: The profiles of the 5th (first row), the 15th (second row), and the 22nd (third row) estimated interplies respectively. The interplies are estimated from the 50 MHz LP filtered signals (first column), the 15 MHz deconvolved signals (second column), and the 5 MHz analytic-signals (third column) respectively.

mentioned techniques. The images of the depth profiles reconstructed by the 50 MHz LP filtered signals are evidently very noisy. One could say that the profile of the 5th interply can be extracted, though with low quality. The 15 MHz signals with Wiener deconvolution can reconstruct the profiles of the 5th and 15th interplies with higher quality but yield fully unstable results for the 22nd ply. The 5 MHz analytic-signals with log-Gabor filter successfully reconstruct the depth profile of all the interplies with high quality. Although, it is clear that the depth profile of the 22nd interply becomes more unsteady and less accurate.

It is important to note that there is an intrinsic difference in the noise level between the different transducers (see Table 4). The higher frequency transducer intrinsically produces more noise due to the electrical power loss as well as the mechanical power loss [66]. Therefore, the low-frequency signals tend to be naturally more stable than the high-frequency signals. This also contributes to worse performance of the 50 MHz and the 15 MHz signals in the experiments. Another potential problem of using high-frequency ultrasound is that it could be sensitive to fiber tows inside the plies [67]. There is an obvious difficulty in reconstructing the positions of the interplies because the echoes from the fiber tows could be mistaken as the echoes from the interplies.

5. Conclusions

This study discussed and compared several ultrasonic techniques, operating in different frequency ranges, for reconstructing the multilayered structure of composites. The performance of the different ultrasonic techniques is investigated on synthetic ultrasonic data, with various noise levels, a representative for a 24 layer composite immersed in water. It is revealed that the 50 MHz ultrasound with LP filtering, coupled to the analysis of the instantaneous amplitude, can only effectively distinguish the near-surface interplies with good robustness. The 15 MHz ultrasound has better probing depth and yields reasonably stable estimation, especially when it is coupled to Wiener deconvolution. Though, for the deeper interplies the results become unstable and their locations could not be extracted in a robust manner. Finally, the 5 MHz ultrasound coupled to analytic-signal analysis provides the best robustness and probing depth under all noise levels. This approach makes use of the ply-resonance (around 6.5 MHz for the here considered multilayered structure), and evaluates the instantaneous phase in order to estimate the depth of the interplies. This approach yields good results over the full depth of the considered multilayered structure, especially when coupled to a log-Gabor filter for optimal scaling of the signals. However, the analytic-signal results also indicate a systematic deviation in the depth estimation of the two interplies closest to the front- and back surface. This is attributed to the dominating effect of the front- and back-wall echo which locally distorts the instantaneous phase profile.

Also, an experimental study on a $[45/0/-45/90]_{3s}$ CFRP sample with 24 plies is reported. The CFRP sample has been raster-scanned in pulse-echo mode with several transducers operating in different frequency ranges. The estimated interply locations are displayed in B-scan mode, and the extracted ply thicknesses are compared with the nominal ply thickness. The profiles of the estimated interplies at several depths are displayed in C-scan mode. The obtained experimental results fully confirm the observations and results from the simulation study.

The comparative analysis of this research provides deeper insights into the performance of the ultrasonic techniques operating in different frequency ranges. It could serve as a base for selecting the appropriate ultrasonic techniques for reconstructing the multilayered structure of composite laminates.

6. Acknowledgment

This work is supported by China Scholarship Council and Ghent University Preference CSC program (No. 01SC0219), Bijzonder OnderzoeksFonds Ghent University (BOF 01N01719), ALMA project (HBC.2018.0427) which fits in the research program STREAM funded by SIM (Strategic Initiative Materials in Flanders) and VLAIO (Flemish government agency Innovation & Entrepreneurship), and the National Natural Science Foundation of China (No. U1709206).

References

[1] Karataş, M.A., Gökkaya, H.. A review on machinability of carbon fiber reinforced polymer (cfrp) and glass fiber reinforced polymer (gfrp) composite materials. Def Technol 2018;14(4):318–326. doi:https://doi.org/10.1016/j.dt.2018.02.001.

[2] Rajak, D.K., Pagar, D.D., Menezes, P.L., Linul, E.. Fiber-reinforced polymer composites: Manufacturing, properties, and applications. Polymers 2019;11(10):1667. doi:https://doi.org/10.3390/polym11101667.

[3] Amafabia, D.M., Montalvão, D., David-West, O., Haritos, G.. A review of structural health monitoring techniques as applied to composite structures. SDHM 2018;11(2):91–147. doi:https://doi.org/10.3970/sdhm.2017.011.091.

[4] Linul, E., Vălean, C., Linul, P.A.. Compressive behavior of aluminum microfibers reinforced semi-rigid polyurethane foams. Polymers 2018;10(12):1298. doi:https://doi.org/10.3390/polym10121298.
[5] Chukov, D., Nematulloev, S., Torokhov, V., Stepashkin, A., Sherif, G., Tcherdyntsev, V.. Effect of carbon fiber surface modification on their interfacial interaction with polysulfone. Results Phys 2019;15:102634. doi:https://doi.org/10.1016/j.rinp.2019.102634.
[6] Wang, B., Zhong, S., Lee, T.L., Fancey, K.S., Mi, J.. Non-destructive testing and evaluation of composite materials/structures: A state-of-the-art review. Adv Mech Eng 2020;12(4):1687814020913761. doi:https://doi.org/10.1177/1687814020913761.
[7] Gholizadeh, S.. A review of non-destructive testing methods of composite materials. Procedia Structural integr 2016;1:50–57. doi:https://doi.org/10.1016/j.prostr.2016.02.008.
[8] Duchene, P., Chaki, S., Ayadi, A., Krawczak, P.. A review of non-destructive techniques used for mechanical damage assessment in polymer composites. J Mater Sci 2018;53(11):7915–7938. doi:https://doi.org/10.1007/s10853-018-2045-6.
[9] Emerson, M.J., Jespersen, K.M., Dahl, A.B., Conradsen, K., Mikkelsen, L.P.. Individual fibre segmentation from 3d x-ray computed tomography for characterising the fibre orientation in unidirectional composite materials. Compos Part A Appl Sci Manuf 2017;97:83–92. doi:https://doi.org/10.1016/j.compositesa.2016.12.028.
[10] Park, D.W., Oh, G.H., Kim, D.J., Kim, H.S.. In-situ thickness measurement of epoxy molding compound in semiconductor package products using a terahertz-time of flight system. NDT E Int 2019;105:11–18. doi:https://doi.org/10.1016/j.ndteint.2019.04.012.
[11] Park, D.W., Oh, G.H., Kim, H.S.. Predicting the stacking sequence of e-glass fiber reinforced polymer (gfrp) epoxy composite using terahertz time-domain spectroscopy (thz-tds) system. Compos B Eng 2019;177:107385. doi:https://doi.org/10.1016/j.compositesb.2019.107385.
[12] Meola, C., Carlomagno, G.M.. Infrared thermography to evaluate impact damage in glass/epoxy with manufacturing defects. Int J Impact Eng 2014;67:1–11. doi:https://doi.org/10.1016/j.ijimpeng.2013.12.010.
[13] Poelman, G., Hedayatrasa, S., Segers, J., Van Paepegem, W., Kersemans, M.. Adaptive spectral band integration in flash thermography: Enhanced defect detectability and quantification in composites. Compos B Eng 2020;202:108305. doi:https://doi.org/10.1016/j.compositesb.2020.108305.
[14] De Angelis, G., Meo, M., Almond, D.P., Pickering, S.G., Angioni, S.L.. A new technique to detect defect size and depth in composite structures using digital shearography and unconstrained optimization. NDT E Int 2012;45(1):91–96. doi:https://doi.org/10.1016/j.ndteint.2011.07.007.
[15] Mizukami, K., Mizutani, Y., Kimura, K., Sato, A., Todoroki, A., Suzuki, Y.. Detection of in-plane fiber waviness in cross-ply cfrp laminates using layer selectable eddy current method. Compos Part A Appl Sci Manuf 2016;82:108–118. doi:https://doi.org/10.1016/j.compositesa.2015.11.040.
[16] Mizukami, K., Mizutani, Y., Todoroki, A., Suzuki, Y.. Detection of in-plane and out-of-plane fiber waviness in unidirectional carbon fiber reinforced composites using eddy current testing. Compos B Eng 2016;86:84–94. doi:https://doi.org/10.1016/j.compositesb.2015.09.041.
[17] Harizi, W., Chaki, S., Bourse, G., Ourak, M.. Mechanical damage characterization of glass fiber-reinforced polymer laminates by ultrasonic maps. Compos B Eng 2015;70:131–137. doi:https://doi.org/10.1016/j.compositesb.2014.11.014.
[18] Kersemans, M., Martens, A., Lammens, N., Van Den Abeele, K., Degrieck, J., Zastavnik, F., et al. Identification of the elastic properties of isotropic and orthotropic thin-plate materials with the pulsed ultrasonic polar scan. Exp Mech 2014;54(6):1121–1132. doi:https://doi.org/10.1007/s11340-014-9861-7.
[19] Song, H., Yang, Y.. Super-resolution visualization of subwavelength defects via deep learning-enhanced ultrasonic beamforming: A proof-of-principle study. NDT E Int 2020;116:102344. doi:https://doi.org/10.1016/j.ndteint.2020.102344.
[20] Shoukroun, D., Massimi, L., Iacoviello, F., Endrizzi, M., Bate, D., Olivo, A., et al. Enhanced composite plate impact damage detection and characterisation using x-ray refraction and scattering contrast combined with ultrasonic imaging. Compos B Eng 2020;181:107579. doi:https://doi.org/10.1016/j.compositesb.2019.107579.
[21] Blandford, B.M., Jack, D.A.. High resolution depth and area measurements of low velocity impact damage in carbon fiber laminates via an ultrasonic technique. Compos B Eng 2020;188:107843. doi:https://doi.org/10.1016/j.compositesb.2020.107843.
[22] Caminero, M., García-Moreno, I., Rodríguez, G., Chacón, J.. Internal damage evaluation of composite structures using phased array ultrasonic technique: Impact damage assessment in cfrp and 3d printed reinforced composites. Compos B Eng 2019;165:131–142. doi:https://doi.org/10.1016/j.compositesb.2018.11.091.
[23] Wronkowicz, A., Dragan, K., Lis, K.. Assessment of uncertainty in damage evaluation by ultrasonic testing of composite structures. Compos Struct 2018;203:71–84. doi:https://doi.org/10.1016/j.compstruct.2018.06.109.
[24] Morokov, E., Levin, V., Chernov, A., Shanygin, A.. High resolution ply-by-ply ultrasound imaging of impact damage in thick cfrp laminates by high-frequency acoustic microscopy. Compos Struct 2021;256:113102.
[25] Wang, D., He, X., Xu, Z., Jiao, W., Yang, F., Jiang, L., et al. Study on damage evaluation and machinability of ud-cfrp for the orthogonal cutting operation using scanning acoustic microscopy and the finite element method. Materials 2017;10(2):204. doi:https://doi.org/10.3390/ma10020204.
[26] Bai, X., Sun, Z., Sun, A., Chen, J., Ju, B.F.. Determination of the multiple local properties of thin layer with high lateral resolution by scanning acoustic microscopy. Rev Sci Instrum 2014;85(9):094901. doi:https://doi.org/10.1063/1.4894261.
[27] Ono, K.. A comprehensive report on ultrasonic attenuation of engineering materials, including metals, ceramics, polymers, fiber-reinforced composites, wood, and rocks. Appl Sci 2020;10(7):2230. doi:https://doi.org/10.3390/app10072230.
[28] Mohammadkhani, R., Zanotti Fragonara, L., Padiyar M, J., Petrunin, I., Raposo, J., Tsourdos, A., et al. Improving depth resolution of ultrasonic phased array imaging to inspect aerospace composite structures. Sensors 2020;20(2):559. doi:https://doi.org/10.3390/s20020559.
[29] Abdessalem, B., Ahmed, K., Redouane, D.. Signal quality improvement using a new tmsse algorithm: Application in delamination detection in composite materials. J Nondestr Eval 2017;36(1):16. doi:https://doi.org/10.1007/s10921-017-0398-4.

[30] Burrows, S.E., Fan, Y., Dixon, S.. High temperature thickness measurements of stainless steel and low carbon steel using electromagnetic acoustic transducers. NDT E Int 2014;68:73–77. doi:https://doi.org/10.1016/j.ndteint.2014.07.009.
[31] Losada, R.A.. Practical fir filter design in matlab. The Math Works inc Revision 2004;1:5–26.
[32] Sin, S.K., Chen, C.H.. A comparison of deconvolution techniques for the ultrasonic nondestructive evaluation of materials. IEEE Trans Image Process 1992;1(1):3–10. doi:https://doi.org/10.1109/83.128026.
[33] Neal, S.P., Speckman, P.L., Enright, M.. Flaw signature estimation in ultrasonic nondestructive evaluation using the wiener filter with limited prior information. IEEE Trans Ultrason Ferroelectr Freq Control 1993;40(4):347–353. doi:https://doi.org/10.1109/58.251283.
[34] Miyashita, T., Schwetlick, H., Kessel, W.. Recovery of ultrasonic impulse response by spectral extrapolation. In: Acoustical Imaging. Springer; 1985, p. 247–257. doi:https://doi.org/10.1007/978-1-4613-2523-9_23.
[35] Zala, C., Barrodale, I., McRae, K.. High resolution deconvolution of ultrasonic traces. In: Signal processing and pattern recognition in nondestructive evaluation of materials. Springer; 1988, p. 101–108. doi:https://doi.org/10.1007/978-3-642-83422-6_7.
[36] Honarvar, F., Sheikhzadeh, H., Moles, M., Sinclair, A.N.. Improving the time-resolution and signal-to-noise ratio of ultrasonic nde signals. Ultrasonics 2004;41(9):755–763. doi:https://doi.org/10.1016/j.ultras.2003.09.004.
[37] Karslı, H.. Further improvement of temporal resolution of seismic data by autoregressive (ar) spectral extrapolation. J Appl Geophy 2006;59(4):324–336. doi:https://doi.org/10.1016/j.jappgeo.2005.11.001.
[38] Wei, L., Huang, Z.y., Que, P.w.. Sparse deconvolution method for improving the time-resolution of ultrasonic nde signals. NDT E Int 2009;42(5):430–434. doi:https://doi.org/10.1016/j.ndteint.2009.01.009.
[39] Wiggins, R.A.. Minimum entropy deconvolution. Geoexploration 1978;16(1-2):21–35. doi:https://doi.org/10.1016/0016-7142(78)90005-4.
[40] Lee, J.Y., Nandi, A.. Extraction of impacting signals using blind deconvolution. J Sound Vib 2000;232(5):945–962. doi:https://doi.org/10.1006/jsvi.1999.2778.
[41] Nandi, A.K., Mampel, D., Roscher, B.. Blind deconvolution of ultrasonic signals in nondestructive testing applications. IEEE Trans Signal Process 1997;45(5):1382–1390. doi:https://doi.org/10.1109/78.575716.
[42] Boßmann, F., Plonka, G., Peter, T., Nemitz, O., Schmitte, T.. Sparse deconvolution methods for ultrasonic ndt. J Nondestr Eval 2012;31(3):225–244. doi:https://doi.org/10.1007/s10921-012-0138-8.
[43] Chang, Y., Zi, Y., Zhao, J., Yang, Z., He, W., Sun, H.. An adaptive sparse deconvolution method for distinguishing the overlapping echoes of ultrasonic guided waves for pipeline crack inspection. Meas Sci Technol 2017;28(3):035002. doi:http://dx.doi.org/10.1088/1361-6501/aa52ae.
[44] Smith, R.A., Nelson, L.J., Mienczakowski, M.J., Wilcox, P.D.. Ultrasonic analytic-signal responses from polymer-matrix composite laminates. IEEE Trans Ultrason Ferroelectr Freq Control 2017;65(2):231–243. doi:https://doi.org/10.1109/TUFFC.2017.2774776.
[45] Nelson, L., Smith, R., Mienczakowski, M.. Ply-orientation measurements in composites using structure-tensor analysis of volumetric ultrasonic data. Compos Part A Appl Sci Manuf 2018;104:108–119. doi:https://doi.org/10.1016/j.compositesa.2017.10.027.
[46] Nelson, L., Smith, R.. Fibre direction and stacking sequence measurement in carbon fibre composites using radon transforms of ultrasonic data. Compos Part A Appl Sci Manuf 2019;118:1–8. doi:https://doi.org/10.1016/j.compositesa.2018.12.009.
[47] Yang, X., Verboven, E., Ju, B.f., Kersemans, M.. Parametric study on interply tracking in multilayer composites by analytic-signal technology. Ultrasonics 2021;111:106315. doi:https://doi.org/10.1016/j.ultras.2020.106315.
[48] Smith, R.A., Nelson, L.J., Mienczakowski, M.J., Wilcox, P.D.. Ultrasonic tracking of ply drops in composite laminates. In: AIP Conference Proceedings; vol. 1706. AIP Publishing LLC; 2016, p. 050006.
[49] Neal, S.P., Thompson, D.O.. A prior knowledge based optimal wiener filtering approach to ultrasonic scattering amplitude estimation. J Acoust Soc Am 1989;86(S1):S94–S94. doi:https://doi.org/10.1121/1.2027743.
[50] Ulrych, T.J., Bishop, T.N.. Maximum entropy spectral analysis and autoregressive decomposition. Rev Geophys 1975;13(1):183–200. doi:https://doi.org/10.1029/RG013i001p00183.
[51] Shakibi, B.. Resolution enhancement of ultrasonic signals using autoregressive spectral extrapolation. Ph.D. thesis; 2011.
[52] Bridge, C.P.. Introduction to the monogenic signal. 2017. arXiv:1703.09199.
[53] Field, D.J.. Relations between the statistics of natural images and the response properties of cortical cells. J Opt Soc Am A 1987;4(12):2379–2394. doi:https://doi.org/10.1364/JOSAA.4.002379.
[54] Boukerroui, D., Noble, J.A., Brady, M.. On the choice of band-pass quadrature filters. J Math Imaging Vis 2004;21(1-2):53–80. doi:https://doi.org/10.1023/B:JMIV.0000026557.50965.09.
[55] Brekhovskikh, L.M.. Waves in layered media. New York: Academic Press; 1960, p. 22–26.
[56] Cann, M.T., Adams, D.O., Schneider, C.L.. Characterization of fiber volume fraction gradients in composite laminates. J Compos Mater 2008;42(5):447–466. doi:https://doi.org/10.1177/0021998307086206.
[57] Hallal, A., Younes, R., Fardoun, F., Nehme, S.. Improved analytical model to predict the effective elastic properties of 2.5 d interlock woven fabrics composite. Compos Struct 2012;94(10):3009–3028. doi:https://doi.org/10.1016/j.compstruct.2012.03.019.
[58] Sevenois, R., Garoz, D., Verboven, E., Spronk, S., Gilabert, F., Kersemans, M., et al. Multiscale approach for identification of transverse isotropic carbon fibre properties and prediction of woven elastic properties using ultrasonic identification. Compos Sci Technol 2018;168:160–169. doi:https://doi.org/10.1016/j.compscitech.2018.09.016.
[59] Davila, Y., Crouzeix, L., Douchin, B., Collombet, F., Grunevald, Y.H.. Spatial evolution of the thickness variations over a cfrp laminated structure. Appl Compos Mater 2017;24(5):1201–1215. doi:https://doi.org/10.1007/s10443-016-9573-5.
[60] Collombet, F., Mulle, M., Grunevald, Y.H., Zitoune, R.. Contribution of embedded optical fiber with bragg grating in composite structures for tests-simulations dialogue. Mech Adv Mater Struct 2006;13(5):429–439. doi:https://doi.org/10.1080/15376490600777616.
[61] Smith, R.A.. Use of 3d ultrasound data sets to map the localised properties of fibre-reinforced composites. Ph.D. thesis; University of Nottingham; 2010.
[62] Jeong, H., Hsu, D.K.. Experimental analysis of porosity-induced ultrasonic attenuation and velocity change in carbon composites. Ultrasonics

1995;33(3):195–203. doi:https://doi.org/10.1016/0041-624X(95)00023-V.

[63] Shakibi, B., Honarvar, F., Moles, M., Caldwell, J., Sinclair, A.N.. Resolution enhancement of ultrasonic defect signals for crack sizing. NDT E Int 2012;52:37–50. doi:https://doi.org/10.1016/j.ndteint.2012.08.003.

[64] Joliff, Y., Bélec, L., Heman, M., Chailan, J.F.. Experimental, analytical and numerical study of water diffusion in unidirectional composite materials–interphase impact. Comput Mater Sci 2012;64:141–145. doi:https://doi.org/10.1016/j.commatsci.2012.05.029.

[65] Peret, T., Clement, A., Freour, S., Jacquemin, F.. Homogenization of fickian and non-fickian water diffusion in composites reinforced by hydrophobic long fibers: Application to the determination of transverse diffusivity. Compos Struct 2019;226:111191. doi:https://doi.org/10.1016/j.compstruct.2019.111191.

[66] Karafi, M.R., Khorasani, F.. Evaluation of mechanical and electric power losses in a typical piezoelectric ultrasonic transducer. Sens Actuators A Phys 2019;288:156–164. doi:https://doi.org/10.1016/j.sna.2018.12.044.

[67] Moon, M., Yun, Y., Yoo, M., Song, J., Oh, J.. Carbon fiber manufacturing and applications as a benchmark for nanotube superfiber development. In: Nanotube Superfiber mater. Elsevier; 2019, p. 879–896. doi:https://doi.org/10.1016/B978-0-12-812667-7.00034-3.

Comparative study of ultrasonic techniques for reconstructing the multilayer structure of composites

Xiaoyu Yang[a,b,*,1], Erik Verboven[a], Bing-feng Ju[b] and Mathias Kersemans[a,*]

[a]Mechanics of Materials and Structures (UGent-MMS), Ghent University, Ghent, Belgium
[b]The State Key Laboratory of Fluid Power Transmission and Control, Zhejiang University, Hangzhou, People's Republic of China

ARTICLE INFO

Keywords:
ultrasonics testing
comparative study
deconvolution technique
analytic-signal
multilayer composite
interply track

ABSTRACT

The multilayer structure of fiber-reinforced polymers may be extracted by ultrasonic pulse-echo inspection. Depending on the employed ultrasonic frequency and subsequent processing methodology, different depth resolution and dynamic depth range can be achieved. This study compares the performance of different ultrasonic pulse-echo approaches for extracting the ply-by-ply structure of multilayered composites. The following methodologies are studied: Method 1: 50 MHz, 15 MHz, and 5 MHz ultrasound with low-pass filtering using analysis of the instantaneous amplitude, Method 2: 15 MHz ultrasound with Wiener deconvolution (and AR spectral extrapolation) using analysis of the instantaneous amplitude, and Method 3: 5 MHz ultrasound with low-pass or log-Gabor filtering using analysis of the instantaneous phase. In the simulation study, the performance of the various techniques are investigated on synthetic data representative for a 24-ply carbon fiber reinforced polymer. The robustness of the techniques is evaluated for different signal-to-noise ratios. The various techniques are further investigated on experimental data of a 24-ply cross-ply carbon fiber reinforced polymer. The ply-by-ply structure is extracted and presented in the form of both B-scan and C-scan images. The thickness of each ply is estimated for quantitative analysis. The obtained results indicate that the 5 MHz ultrasound coupled to analytic-signal analysis with log-Gabor filter shows the best performance for reconstructing the multilayer structure of the studied composites.

1. Introduction

Carbon and glass fiber-reinforced polymers (CFRP and GFRP) are widely used in contemporary applications, including space and aviation, automotive, and maritime [1, 2] because of their high specific stiffness (strength) and good corrosion resistance amongst others [3, 4, 5]. To ensure the quality and structural integrity of composite materials, non-destructive testing (NDT) methods can be used [6]. NDT methods play a critical role in the evaluation and maintenance of composite materials. A wide variety of NDT techniques has been built on different principles [7, 8], including x-ray computed tomography [9], terahertz testing [10, 11], infrared thermography [12, 13], shearography [14], eddy current testing [15, 16], ultrasonic testing (UT) [17, 18, 19], etc.

Among the various NDT techniques, UT has been most commonly used for the inspection of multilayer composites [20, 21, 22]. A major advantage of using UT is that it is highly sensitive to the multilayered structure and various damage types commonly found in composites [23]. High-frequency ultrasound can be utilized for the characterization of sub-surface damage with a high spatial and temporal resolution [24, 25, 26]. As the thickness and the number of plies increases, the attenuation of high-frequency ultrasound becomes a concern, especially for high damping fiber-reinforced composites [27]. A recent study reported the inspection of an impacted CFRP laminate using 50 MHz ultrasound and demonstrated a depth probing as deep as 2-2.5 mm [24]. Alternatively, one could lower the ultrasound frequency in order to increase the dynamic depth range, but this is at the expense of the depth resolution. Therefore, researchers have employed various signal processing steps to improve the temporal resolution of the ultrasonic response signal [28, 29].

A simple approach concerns the application of a low-pass (LP) filter to reduce the high-frequency noise [30, 31]. Another common signal processing step is the deconvolution technique in order to estimate the impulse response from the recorded signal in the presence of noise. Some studies have been conducted to compare various deconvolution

*Corresponding author
Email: Xiaoyu.Yang@Ugent.be (X. Yang); Mathias.Kersemans@Ugent.be (M. Kersemans)
ORCID(s): 0000-0002-8019-4284 (X. Yang)

techniques and found that Wiener filtering-based techniques yield good results for online applications [32, 33]. However, a major problem with the Wiener filter is that it produces a deconvolved signal with a narrowband spectrum. Naturally, the signal with a narrowband spectrum has a decreased temporal resolution. Therefore, it was proposed to additionally use an autoregressive (AR) spectral extrapolation [34, 35, 36]. In the application of the AR spectral extrapolation, the deconvolved spectrum with a high signal-to-noise ratio (SNR) is modeled as an AR process, which is then used to extrapolate the low SNR part of the signal spectrum. The combination of the Wiener deconvolution and AR spectral extrapolation in the frequency domain improves temporal resolution and SNR further [37]. This method, however, suffers from the fact that the optimized parameters need to be found through trial and error [36, 37]. Further, the Wiener deconvolution is not valid when both the input signal and the system are unknown [38]. Based on the fact that the input signal typically has a sparse distribution, it has been proposed to find a deconvolution filter whose output distribution is as sparse as possible [39, 40]. Several of such blind deconvolution methods have been developed in order to improve the temporal resolution of the ultrasonic signal [41, 42, 43]. However, note that such blind deconvolution is seldom considered in ultrasonic testing because the impulse response function of an employed ultrasonic system is often well known (or can be easily measured).

Recently, it was proposed to employ an ultrasonic frequency around the ply resonance frequency [44]. Hence, this results in a procedure with a low operating frequency and as such yields a high probing depth in multilayer composites [45, 46]. It was indicated that the instantaneous phase of the analytic-signal becomes locked to the interfaces between plies in certain circumstances. It has been also shown that the phase is more stable than the amplitude for tracking plies, especially when the amplitude is affected by the strong surface echoes [44]. To ensure the accuracy and stability of the phase-derived interply tracking, it is required to fulfill several conditions. The most important condition concerns the use of a pulse with a center frequency that is close to the fundamental ply-resonance frequency. Further, an appropriate bandwidth is required to cope with the various thickness. Too narrow bandwidth cannot cope with variations in ply thickness, while a too wide bandwidth might excite a strong second-harmonic ply resonance, resulting in wrong depth estimations [44, 47, 48]. Furthermore, the application of a log-Gabor filter has been presented to make the phase-derived interply tracking more stable and robust [47].

This study compares the performance of the different ultrasonic approaches for extracting the ply-by-ply structure of composites:

Method 1: 50 MHz, 15 MHz, and 5 MHz ultrasound with LP filtering, using analysis of the instantaneous amplitude,
Method 2: 15 MHz ultrasound with Wiener deconvolution (and AR spectral extrapolation), using analysis of the instantaneous amplitude,
Method 3: 5 MHz ultrasound with LP or log-Gabor filtering, using analysis of the instantaneous phase.

Note that the 5 MHz is a frequency which is commonly used in industry for inspections of aerospace components. Hence, Method 3 can be directly transferred to such an inspection environment without having to change any hardware, or having to scan the parts multiple times.

This paper is organized as follows. Section 2 describes the theoretical framework of the signal processing techniques, including the LP filtering, the deconvolution technique and the analytic-signal technique. Sections 3.1 and 3.2 introduce the analytical model and the used parameters in the simulation. The quantitative evaluation metrics are proposed and described in section 3.3. Sections 3.4 and 3.5 investigate the performance of the different techniques for the synthetic data with different SNR. The experimental results are discussed in section 4. Finally, section 5 presents the conclusions.

2. Background

Finite impulse response (FIR) filters are widely used for LP filtering due to their inherent stability when implemented in non-recursive form and simple extensibility to multi-rate cases. In this study, a FIR LP filter is applied as a pre-processing step to the recorded signals in order to reduce noise features [31]. The cutoff frequency of the FIR LP filter is twice the center frequency of the employed ultrasonic pulse. The transition band steepness is 0.8 and the stopband attenuation is 60 dB.

2.1. Wiener deconvolution with spectral extrapolation

In a linear time-invariant (LTI) system, the response signal $y(t)$ can be modeled as the convolution of the input signal $h(t)$ with the reflection sequence of the specimen $x(t)$, plus the addition of noise $n(t)$ (see Fig. 1):

$$y(t) = x(t) * h(t) + n(t), \tag{1}$$

where $*$ denotes the convolution operator. Eq. (1) can be expressed in the frequency domain as follows:

$$Y(\omega) = X(\omega)H(\omega) + N(\omega), \tag{2}$$

where $Y(\omega)$, $X(\omega)$, $H(\omega)$, and $N(\omega)$ represent the Fourier transforms of $y(t)$, $x(t)$, $h(t)$, and $n(t)$ respectively.

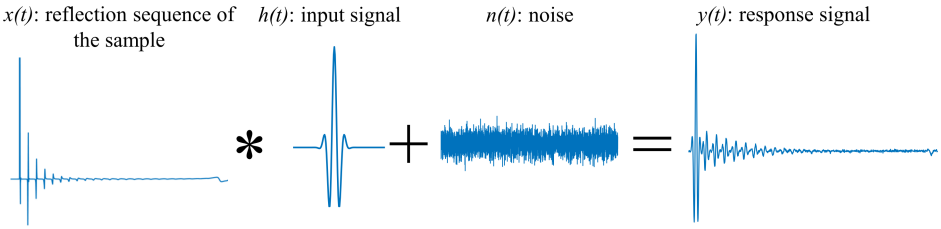

Figure 1: The response signal $y(t)$ from the LTI testing system as the convolution of the input signal $h(t)$ with the reflection sequence of the 24-layer structure $x(t)$ plus the addition of noise $n(t)$. The input signal $h(t)$ has a center frequency of 15 MHz and a fractional bandwidth (-6 dB) of 0.8. The scaling of these waveforms is different both in horizontal (time) and vertical (amplitude) directions.

Considering that $y(t)$ is measured and $h(t)$ is known, a deconvolution procedure can be performed to obtain the deconvolved signal $x_e(t)$ in the presence of noise $n(t)$. To reduce the impact of noise or measurement error, a Wiener filtering in the frequency domain can be applied. A common approach of the Wiener deconvolution can be formulated as [33]

$$X_e(\omega) = \frac{Y(\omega)H^*(\omega)}{|H(\omega)|^2 + Q^2}, \tag{3}$$

where $X_e(\omega)$ represents the Fourier transforms of $x_e(t)$ and Q is the noise desensitizing factor. A commonly recommended value for Q^2 is applied in this study [49, 33]:

$$Q^2 = 10^{-2}|H(\omega)|^2_{\max}, \tag{4}$$

where $|H(\omega)|_{\max}$ is the maximum amplitude of $|H(\omega)|$. The final stage is to employ the inverse Fourier transform to obtain the deconvolved signal in the time domain:

$$x_e(t) = IFT(X_e(\omega)), \tag{5}$$

where $IFT(\bullet)$ denotes the inverse Fourier transform.

To improve the temporal resolution further, AR spectral extrapolation can be applied to the reflection spectrum $X_e(\omega)$ obtained by Wiener filtering. First, a certain bandwidth of the measured reflection spectrum with a high SNR should be selected, whose lower and upper bounds are f_1 and f_2 respectively. The maximum-entropy algorithm of Burg [50] is then used to calculate the AR coefficients from the selected frequency window. Based on the high SNR reflection spectrum, the lower and upper parts of the reflection spectrum are extrapolated as follows:

$$\hat{X}_e(m) = -\sum_{k=1}^{p} a_k X_e(m+k) \quad m = 1, 2, \ldots, \frac{Nf_1}{f_s} - 1, \tag{6}$$

$$\hat{X}_e(n) = -\sum_{k=1}^{p} a_k^* X_e(n-k) \quad n = \frac{Nf_2}{f_s} + 1, \ldots, \frac{N}{2}, \tag{7}$$

where $\hat{X}_e(m)$ and $\hat{X}_e(n)$ are the lower and upper parts of the extrapolated spectrum respectively, N is the sampling points, f_s is the sampling rate, a_k and a_k^* are the AR coefficients and their complex conjugates, respectively, and p is the order of the AR model.

It has been proposed that the extrapolated signals obtained from different frequency windows could improve the robustness of this technique [36]. Hence, the extrapolated spectra from various frequency windows are averaged prior

to performing the inverse Fourier transform for converting the signal into the time domain. The 3 dB to 10 dB drop frequency windows, which are recommended in literature [36], are applied. Following the selection of the frequency window, the following equation is used to select the optimal order p_{opt} for performing the AR spectral extrapolation (with Burg as the fitting method) [51]:

$$p_{opt} = 0.014SNR + 0.21, \tag{8}$$

where SNR is expressed in decibel. Finally, the inverse Fourier transform can be employed on the extrapolated spectrum to obtain the extrapolated signal in the time domain:

$$\hat{x}_e(t) = IFT(\hat{X}_e(\omega)). \tag{9}$$

2.2. Analytic-signal with log-Gabor filter

The analytic-signal $s_a(t)$ represents a signal in its complex form, which is composed of a real part $s(t)$ (see Fig. 2a), and an imaginary part $g(t)$ as follows:

$$s_a(t) = s(t) + ig(t). \tag{10}$$

The imaginary part $g(t)$ is derived from the real part $s(t)$ by the Hilbert transform:

$$g(t) = \int_{-\infty}^{+\infty} \frac{s(\tau)}{\pi(t-\tau)} d\tau. \tag{11}$$

The complex-valued analytic-signal can be represented by its magnitude and phase (see Fig. 2b). The mathematical form also reads as follows:

$$s_a(t) = A_{inst}(t)e^{i\phi_{inst}(t)}, \tag{12}$$

where $A_{inst}(t) = \sqrt{s^2(t) + g^2(t)}$ and $\phi_{inst}(t) = \arctan\frac{g(t)}{s(t)}$ are the instantaneous amplitude and instantaneous phase, respectively (see Figs. 2c and 2d). The instantaneous frequency $f_{inst}(t)$ is then obtained from the time-derivative of the instantaneous phase $\phi_{inst}(t)$:

$$f_{inst}(t) = \frac{1}{2\pi}\frac{d\phi_{inst}(t)}{dt}. \tag{13}$$

The relationship between a signal and its analytic-signal can be represented in the frequency domain as follows [52]:

$$F_a(\omega) = (1 + sgn(\omega))F(\omega), \tag{14}$$

where $F_a(\omega)$ and $F(\omega)$ are the Fourier spectrum of $s_a(t)$ and $s(t)$ respectively, ω is the angular frequency, and $sgn(\bullet)$ denotes the sign function.

The instantaneous amplitude and instantaneous phase can be used to derive the positions of the resin-rich interplies in a composite laminate, on the condition that the center frequency of the ultrasonic input signal approximately corresponds to the fundamental ply-resonance frequency [44]. The instantaneous amplitude is analyzed to derive the time-of-flight (TOF) of the front- and back-wall echoes. The instantaneous phases of the reflections from the resin-rich interplies appear to be close to $\phi_0 - \frac{\pi}{2}$, where ϕ_0 is the instantaneous phase of the input pulse. And the peaks of instantaneous amplitude can also be used to estimate the locations for the resin-rich interplies. The log-Gabor filter [53] decomposes the analytic-signal in different appropriate scales, and as such provides better estimates for the instantaneous phase and instantaneous frequency [47, 54]. The log-Gabor filter is defined in the frequency domain as follows:

$$G(\omega) = \exp\frac{-(\log\frac{|\omega|}{\omega_0})^2}{2(\log\sigma_0)^2}, \tag{15}$$

where ω_0 is the angular center frequency of the passband, σ_0 is the parameter governing the bandwidth of the passband. The log-Gabor filtered analytic-signal in the frequency domain $\tilde{F}_a(\omega)$ can be obtained by

$$\tilde{F}_a(\omega) = G(\omega)F_a(\omega). \tag{16}$$

Its time-domain representation $\tilde{s}_a(t)$ is then obtained by application of the inverse Fourier transform:

$$\tilde{s}_a(t) = IFT(\tilde{F}_a(\omega)). \tag{17}$$

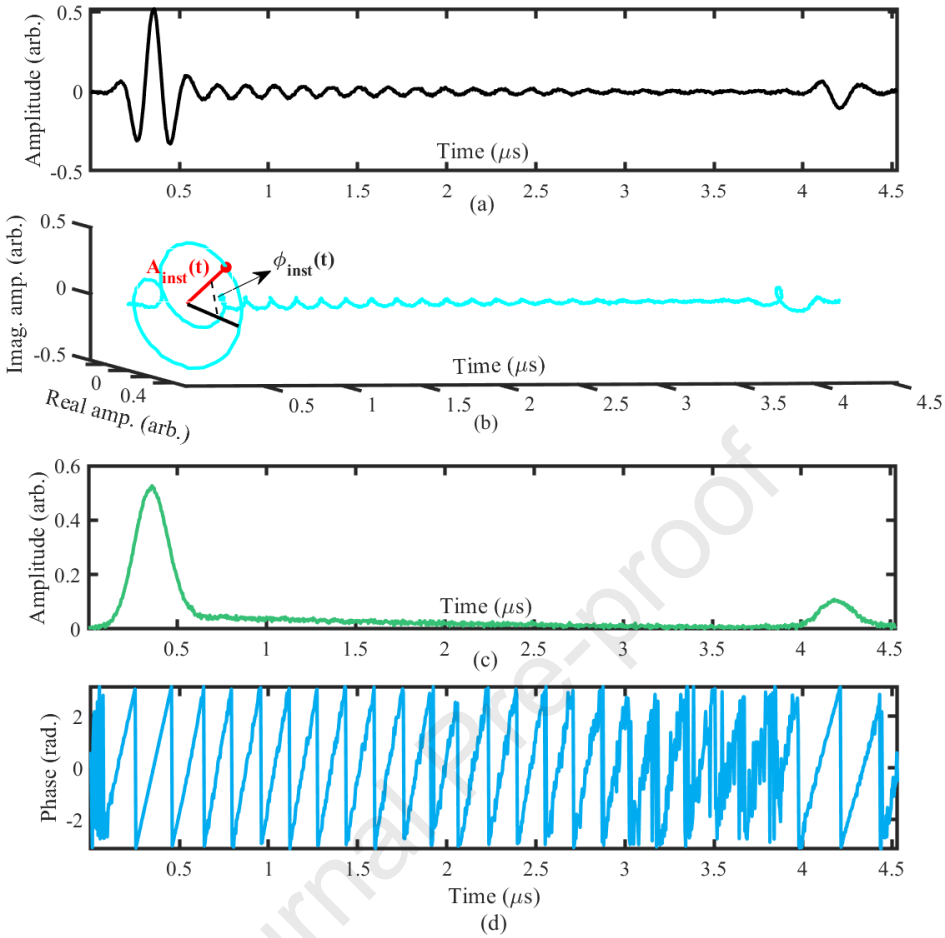

Figure 2: (a) The recorded signal, (b) the analytic-signal in 3-dimensional representation, (c) the instantaneous amplitude, and (d) the instantaneous phase.

3. Simulation study

3.1. Analytical model

The analytical model is implemented in MATLAB. Firstly, the reflection spectrum of the structure is calculated. Secondly, the frequency response is obtained by the multiplication of the Fourier representation of the input signal and the reflection spectrum. Finally, the time-domain reflected signal is obtained and the noise is added. The multilayered structure of a composite laminate immersed in water is illustrated in Fig. 3. The simulated structure consists of 25 interplies (including the front and back surfaces) and 24 plies. Prior to obtaining the complex reflection spectrum of the structure, the acoustic impedance of the n-layered structure is calculated by the recursive method as follows [55]:

$$Z_{\lambda}^{(n)}(\omega) = Z_n \frac{Z_{\lambda}^{(n-1)}(\omega)(e^{2d_n(ik_{zn}-\omega\alpha_n)}+1) - Z_n(e^{2d_n(ik_{zn}-\omega\alpha_n)}-1)}{Z_n(e^{2d_n(ik_{zn}-\omega\alpha_n)}+1) - Z_{\lambda}^{(n-1)}(\omega)(e^{2d_n(ik_{zn}-\omega\alpha_n)}-1)} \quad n \geq 1, \tag{18}$$

where $Z_{\lambda}^{(n)}$ is the total acoustic impedance of the n-layered structure, $Z_n = \rho_n c_{Ln}$ is the acoustic impedance of the nth layer, $k_{zn} = \omega/c_{Ln}$ is the wavenumber in the thickness direction of the nth layer, α_n, d_n, ρ_n, and c_{Ln} are the attenuation, thickness, density, and longitudinal wave velocity of the nth layer respectively. The initial condition is set as $Z_{\lambda}^{(0)} = Z_0$,

which denotes the acoustic impedance of the infinite medium below. The complex reflection spectrum is then obtained as follows:

$$X_s(\omega) = \frac{Z_\lambda^n(\omega) - Z_{n+1}}{Z_\lambda^n(\omega) + Z_{n+1}}, \tag{19}$$

where Z_{n+1} denotes the acoustic impedance of the infinite media above. The reflected signal $y_s^0(t)$ is then obtained as follows:

$$y_s^0(t) = IFT(X_s(\omega)H_s(\omega)), \tag{20}$$

where $H_s(\omega)$ is the complex Fourier representation of the input signal $h_s(t)$. White Gaussian noise $n_s(t)$ is considered which has uniform power over the considered frequency band and normal distribution in the time domain with zero mean value. The reflected signal $y_s(t)$ finally becomes:

$$y_s(t) = y_s^0(t) + n_s(t). \tag{21}$$

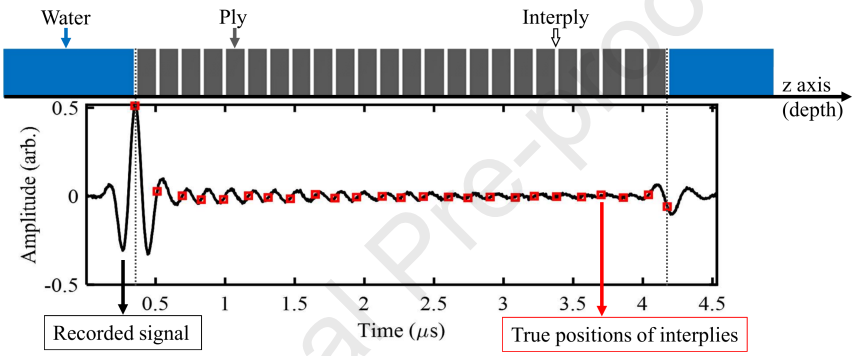

Figure 3: The schematic of the multilayered structure and the signal response.

3.2. Simulation parameters

The interply is considered as a thin epoxy layer of 10 μm with a density of 1270 kg/m^3. The ply is considered as a mixture of unidirectional fibers and epoxy matrix with a fiber volume fraction of 60% [56]. When defining the effective mass density of the ply, the rule of mixture is applied, assuming a density of the carbon fibers of 1800 kg/m^3. The stiffness matrix for each ply is calculated by the Chamis model [57] from the properties of carbon fiber [58] and epoxy matrix. The longitudinal wave velocity propagating in the thickness direction is then calculated from the stiffness matrix. To fully evaluate the performance of the various ultrasonic techniques, a 24-layer laminate with various ply thicknesses is simulated. It is important to consider possible variations in the ply thickness because CFRP plies do not have necessarily a uniform thickness. This variation is mainly introduced during the manufacturing cycle due to resin flow effects before the polymerisation in the autoclave [59, 60]. Hence, a combination of 3 different ply thickness sequences is applied for the simulated data as follows: (i) a uniform ply thickness of 220 μm, (ii) a ply thickness sequence of $[220\mu m/210\mu m/230\mu m]_8$, and (iii) a ply thickness sequence of $[220\mu m/230\mu m/210\mu m]_8$. It is worth noting that the varying ply thickness is more challenging for the analysis of the instantaneous phase due to the fact that it requires a center frequency close to the ply-resonance frequency. Table 1 displays the used properties of the interply, the ply, and the immersion liquid.

The input signal is modeled as a cosine modulated by a Gaussian function:

$$h_s(t) = \exp\left(\frac{t^2 W^2 F_c^2 \pi^2}{4\ln(0.5)}\right)\cos(2\pi F_c t), \tag{22}$$

where t is the time vector, W is the -6 dB fractional bandwidth of the pulse, F_c is the center frequency (see Fig. 4). A nominal SNR of 25 dB is used, which can be considered representative for actual experiments. A sampling rate of 250 MS/s is adopted. Table 2 provides the parameters concerning the input signal and data acquisition.

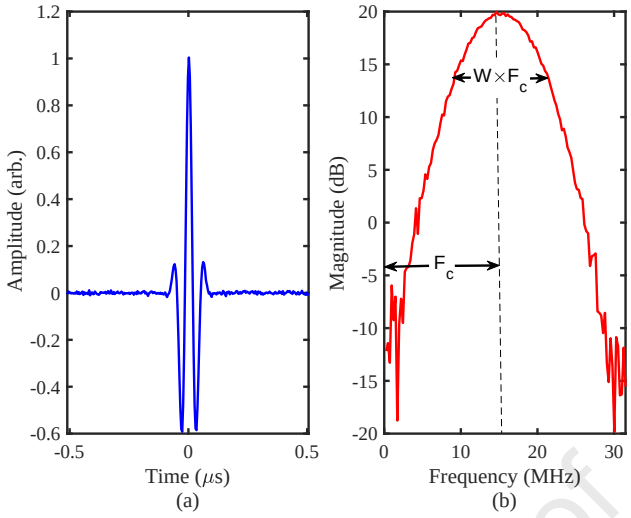

Figure 4: (a) The input signal with a center frequency of 15 MHz and the nominal SNR of 25 dB and (b) its corresponding frequency spectrum.

Table 1
The properties of the interply, the ply, and the immersion liquid.

Name	Materials	Density (kg/m^3)	Thickness (μm)	Wave velocity (m/s)	Attenuation (dB/mm/MHz)
Interply	epoxy	1270 [61]	10	2499 [58]	0.15 [61]
Ply	Mixture of unidirectional fibers and epoxy matrix with a fiber volume fraction of 60%	1588	(i) 220 (ii) $[220/210/230]_8$ (iii) $[220/230/210]_8$	2906	0.1 [62]
Immersion liquid	water	1000		1480	

Table 2
Parameters of the input signal and data acquisition.

Center Frequency (MHz)	-6 dB fractional bandwidth	Bonding media	Nominal SNR (dB)	Sampling rate (MS/s)
5, 15, 50	0.8	water	25	250

3.3. Evaluation metrics

This study uses a quantitative approach to investigate the performance of different ultrasonic techniques. The LP filtered signal is obtained by the application of the LP filter to the original signal $y_s(t)$ in Eq. (21), and the TOF of the interplies is estimated from the local maxima in the instantaneous amplitude (see Fig. 5a). The deconvolved signal equals $x_e(t)$ in Eq. (5) (or $\hat{x}_e(t)$ in Eq. (9) when considering spectral extrapolation), and the TOF of the interplies is estimated from the local maxima in the instantaneous amplitude (see Fig. 5a). The analytic-signal equals $s(t)$ in Eq. (10) (or $\tilde{s}_a(t)$ in Eq. (17) when considering a log-Gabor filter), and the TOF of the interplies is estimated from the instantaneous phase (see Fig. 5b). The detailed procedure for estimating the TOF of the interplies is given in the flowcharts in Fig. 6.

Once the TOF of the interplies are estimated, the error ε^i is calculated as (see also Fig. 5):

$$\varepsilon^i = TOF^i_{est} - TOF^i_{true}, \tag{23}$$

where TOF^i_{est} and TOF^i_{true} are the estimated and the true TOF of the ith interply respectively. The measurement error

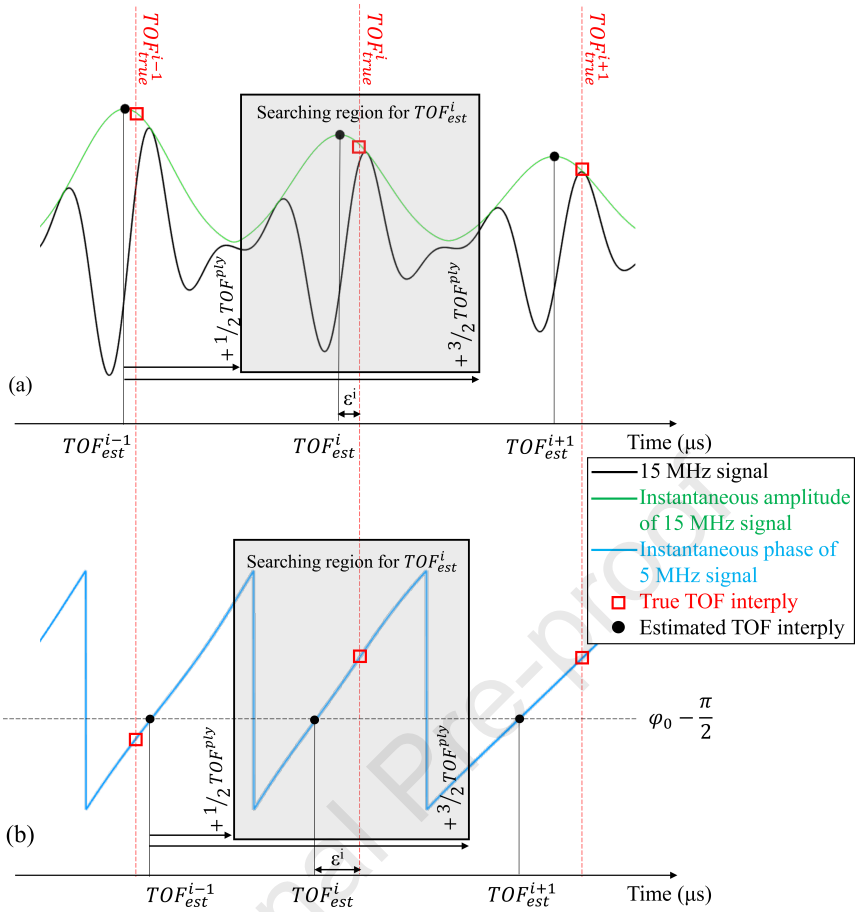

Figure 5: Schematic illustration of TOF estimation of the interplies based on (a) the instantaneous amplitude of a 15 MHz signal, and (b) the instantaneous phase of a 5 MHz signal. Note: the graphs are only for illustration purposes, and do not correspond to real data.

E^i of each interply i is calculated as follows:

$$E^i = \frac{\varepsilon^i}{TOF^{ply}} \times 100[\%], \tag{24}$$

where TOF^{ply} is the true TOF of a single-ply. For each ply thickness sequence, each simulation procedure is repeated 100 times. The statistical information is extracted from the 300 runs in total. The mean measurement errors (ME^i) and the standard deviations of the measurement errors ($STDE^i$) are evaluated:

$$ME^i = \frac{\sum_{j=1}^{N} E^i_j}{N}, \tag{25}$$

$$STDE^i = \sqrt{\frac{\sum_{j=1}^{N}(E^i_j - \overline{E^i_j})^2}{N}}, \tag{26}$$

where E^i_j is the measurement errors E^i in the jth repeat, and N is the number of signals considered.

In general, the ME^i and the $STDE^i$ indicate the accuracy and the robustness for estimating the TOF of the ith interply, respectively. Therefore, the error bars representing the ME^i and the $STDE^i$ can provide a comprehensive evaluation of the performance visually. However, the SNR of the signal is occasionally not high enough for properly distinguishing the interply reflections. In case the TOF^i_{est} is randomly distributed (over the 300 runs) in the searching region and the true TOF of the interply is located in the middle of the searching region, this would result in an ME^i of 0% and an $STDE^i$ of 28.9%, which means the sensitivity to the variations of the ply thickness is completely lost.

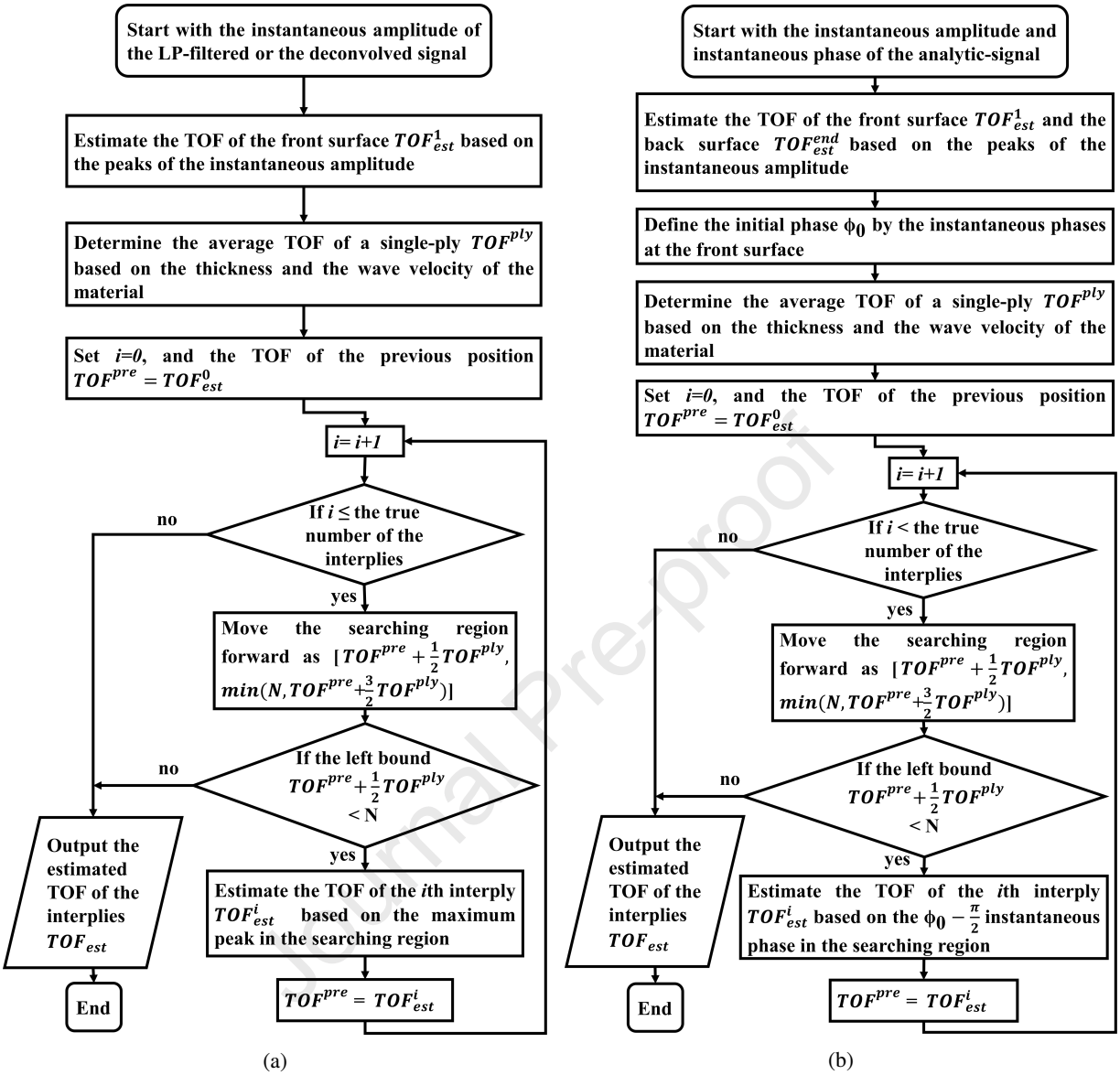

Figure 6: Flowcharts for estimating the TOF of the interplies by using (a) the instantaneous amplitude (Methods 1 and 2) and (b) the instantaneous phase (Method 3).

Hence, to determine whether the interply reflections are distinguishable, a threshold of the $STDE^i$ is set at 22%. The lower the $STDE^i$, the better the interply reflections are distinguishable.

3.4. Results

3.4.1. Low-pass filtered signal using instantaneous amplitude (50 MHz; 15 MHz; 5 MHz)

The resolution and dynamic depth range of an ultrasonic signal are directly linked to its frequency. Fig. 7 displays the simulation results for an input signal with center frequencies of 5 MHz, 15 MHz, and 50 MHz, respectively. The instantaneous amplitudes of the response signals have been extracted by Hilbert transform, from which the positions of the interplies are estimated according to the procedure defined in section 3.3. The true TOF of the interplies are indicated with the vertical dashed lines. From Fig. 7, it becomes clear that a higher center frequency produces sharper peaks at the positions of the interplies, but at the same time experiences more severe attenuation. The ME^i and $STDE^i$ of the estimated interplies are presented in Fig. 8. The front-surface and back-surface interplies are indicated

with F and B respectively. The interplies i are indicated by their depth position, starting from $i = 1$ for the first interply until $i = 23$ for the last interply. If the $STDE^i$ becomes larger than 22% (= interply i could not be distinguished in a proper way), the value for interply i is greyed out.

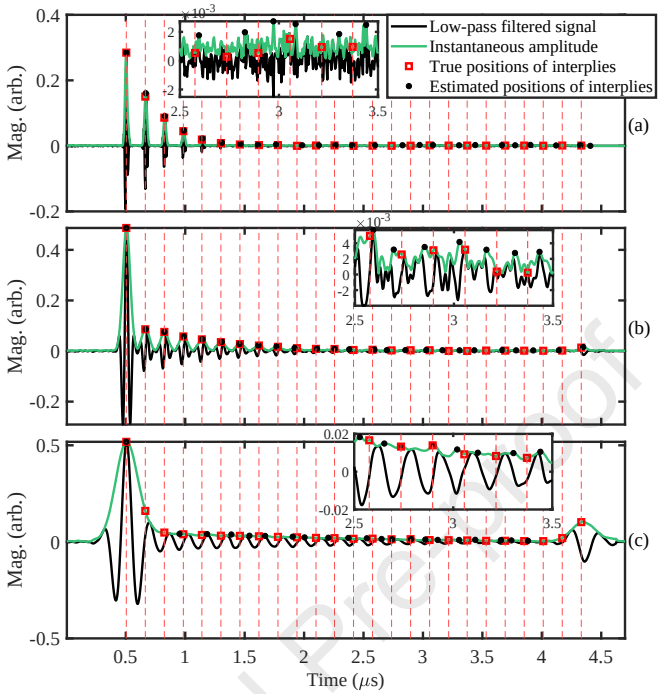

Figure 7: The LP filtered signals with center frequencies of (a) 50 MHz, (b) 15 MHz, and (c) 5 MHz respectively, including the instantaneous amplitude (green trace), and the true and estimated positions of the interplies (red square and black dot respectively).

The 50 MHz LP filtered signal produces sharp and clear peaks for the first 7 interplies, and locates the positions of these interplies in an accurate and robust manner. After the 8th interply, there is a sharp rise in the $STDE^i$. It can also be observed in Fig. 7a that a back-wall echo is not present due to excessive attenuation. Hence, the 50 MHz signal provides high depth resolution in the near-surface plies but becomes impractical due to its low SNR for deeper layers (see also the inset in Fig. 8a).

The 15 MHz LP filtered signal has higher $STDE^i$ for the near-surface plies, but it remains longer stable for deeper layers. The $STDE^i$ remain within 10% for the first 9 interplies. The graph reveals the gradual rise in the $STDE^i$ until it becomes fully unstable for plies deeper than the 14th interply. And an increase in the bias can be seen from the ME^i after the 12th interply. The observed gradual deterioration over depth makes the 15 MHz signal particularly well suited for the deconvolution procedure in order to increase the depth resolution (section 3.4.2).

The 5 MHz ultrasound efficiently penetrates through the whole structure and produces a well-defined back-wall echo. However, the instantaneous amplitude of the 5 MHz LP filtered signal is clearly not valid for extracting the interpliy locations (see Fig. 7c). The amplitude near the surfaces is completely affected by the strong surface echoes. Consequently, no peak of instantaneous amplitude is tracked for the 1st interply (see Fig. 8c). In order to cope with the effects of the front-surface echo on the detection of the 1st interply echo, it is valid to adopt the local minimum of the second derivative of the instantaneous amplitude. Whereas, this procedure is not included in the comparative study since it is non-standard. It can also be seen that the ME^i is very large and $STDE^i$ exceeds the value of 22% instantly. Hence, it may be expected that the application of deconvolution will not provide any significant improvement for the 5 MHz signal. Instead, the 5 MHz signal will be coupled to the analytic-signal analysis, and the instantaneous phase will be used for estimating the positions of the interplies (section 3.4.3).

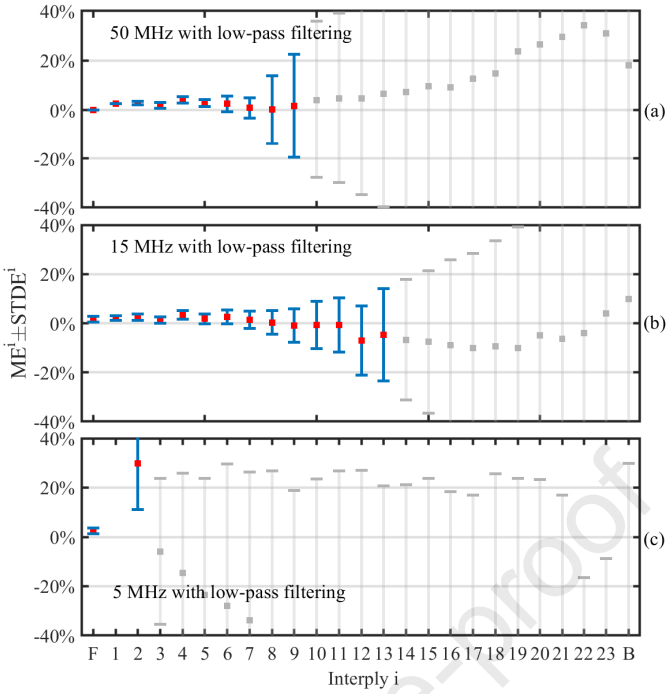

Figure 8: Error bars representing the ME^i and the $STDE^i$ of the estimated interplies from the instantaneous amplitudes of the LP filtered signals with center frequencies of (a) 50 MHz, (b) 15 MHz, and (c) 5 MHz respectively. The data is represented as $ME^i \pm STDE^i$.

3.4.2. Deconvolved signal using instantaneous amplitude (15 MHz)

Based on the response signals (see Figs. 7 and 8), it is anticipated that the application of deconvolution is a practical way to improve the depth resolution for the 15 MHz signal. Fig. 9 displays the deconvolved signal with a center frequency of 15 MHz from Wiener deconvolution and Wiener deconvolution combined with AR spectral extrapolation. The input pulse with the nominal SNR of 25 dB is used as the deconvolution kernel. Table 3 lists the 3 dB to 10 dB drop frequency windows for multiple frequency windows AR spectral extrapolation. The optimal order p_{opt} of the AR process is chosen according to Eq. (8) for each window. The instantaneous amplitudes of the deconvolved signals have been extracted by Hilbert transform, from which the positions of the interplies are estimated according to the previously defined procedure (see section 3.3).

From Fig. 9 it can be seen that the deconvolution techniques improve the temporal resolution and SNR (compared to the 15 MHz LP filtered signal in Fig. 7b). The ME^i and the $STDE^i$ of the estimated interplies from the LP filtered and the deconvolved signals are compared in Fig. 10. Compared to the LP filtered signal, the Wiener deconvolution has a minor effect on the ME^i, but reduces the $STDE^i$ significantly. Hence, this indicates that the extraction of interply locations is more stable and robust. Still, for very deep layers (>17th interply) the $STDE^i$ rapidly converges again to the values above 22%, indicating completely random TOF estimation.

Contrary to the expectation, the deconvolved signal by Wiener filtering with optimized AR spectral extrapolation shows the worst performance of the approaches used in Method 2. This is possibly due to the fact that the AR process is quite sensitive to noise [63]. Further, it has been reported that some spurious spikes could be observed in the deconvolved ultrasonic signal by optimized AR spectral extrapolation [51]. These spurious spikes could be large in amplitude and could become comparable to the actual signal. This is especially valid for the current situation because the reflection signal from the interplies is weak. Hence, the Wiener deconvolution combined with AR spectral extrapolation is not a suitable approach for the here considered case.

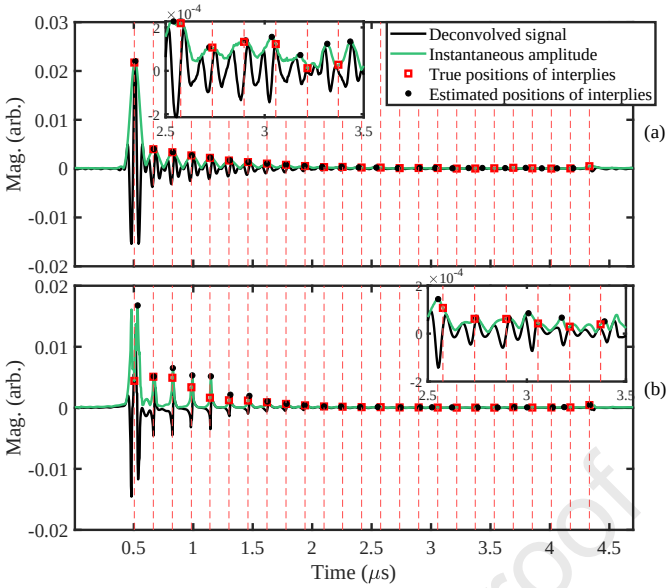

Figure 9: The 15 MHz deconvolved signals by (a) Wiener deconvolution and (b) Wiener deconvolution combined with AR spectral extrapolation respectively, including the instantaneous amplitude (green trace), and the true and estimated positions of the interplies (red square and black dot respectively).

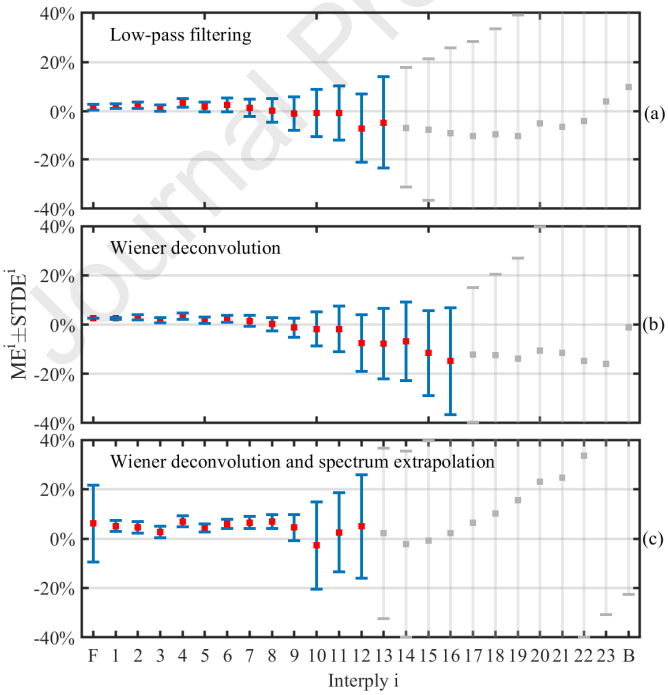

Figure 10: Error bars representing the ME^i and the $STDE^i$ of the estimated interplies from the instantaneous amplitudes of (a) the 15 MHz LP filtered signal, (b) the 15 MHz Wiener deconvolved signal, and (c) the 15 MHz Wiener deconvolved signals combined with AR spectral extrapolation. The data are represented as $ME^i \pm STDE^i$

Table 3
The frequency windows and the optimal orders considered for multiple frequency windows AR spectral extrapolation.

Drop (dB)	Frequency range (MHz)	Data points	p_{opt}
-3	10.8-19.2	88- 158	39
-4	10.1-19.9	83- 163	45
-5	9.5-20.5	78- 168	50
-6	9.0-21.0	74- 172	55
-7	8.5-21.5	70- 176	59
-8	8.1-21.9	66- 180	64
-9	7.7-22.3	63- 183	67
-10	7.3-22.7	59- 186	71

3.4.3. Analytic-signal using instantaneous phase (5 MHz)

From the analysis presented in section 3.4.1, it became clear that the instantaneous amplitude of the 5 MHz LP filtered signal could not be used for estimating the positions of the interplies, except for the front-surface and the back-surface interplies. Considering that the frequency of 5 MHz is close to the ply-resonance frequency, the instantaneous phase could offer an effective way of estimating the positions of the interplies (see section 2.2).

Fig. 11a displays the instantaneous amplitude, instantaneous phase, and instantaneous frequency of the 5 MHz LP filtered analytic-signal. The TOF between the front- and back-wall echoes is approximately 3.8 μs, which indicates a ply-resonance frequency of 6.3 MHz. So 5 MHz is lower than the ply-resonance frequency. However, the instantaneous phase analysis still works here because the bandwidth in the 5 MHz pulse is sufficiently wide in order to excite the 6.3 MHz ply-resonance in an efficient manner. In order to match the input signal better to the ply resonance, a log-Gabor filter is additionally applied for optimal scale selection. The center frequency and σ_0 for the log-Gabor filter are chosen as 6.3 MHz and 0.7, respectively.

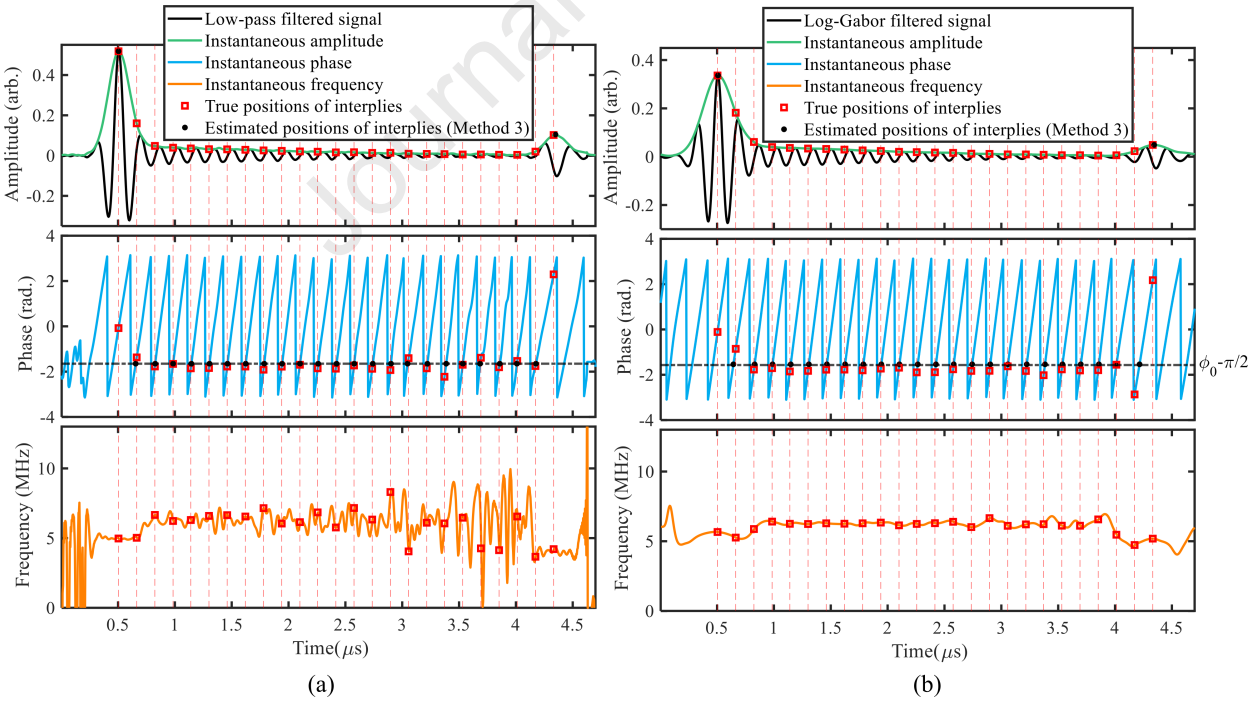

Figure 11: The 5 MHz analytic-signals (a) with LP filtering, and (b) log-Gabor filtering, including the instantaneous amplitude (green trace), the instantaneous phase (blue trace), the instantaneous frequency (orange trace). The true and estimated positions of the interplies are indicated by red squares and black dots respectively.

Fig. 11b displays the instantaneous amplitude, instantaneous phase, and instantaneous frequency of the 5 MHz analytic-signal with the application of the log-Gabor filter. One can readily see the effect of the filter on the quality of the signals, especially on the instantaneous frequency. Compared to the LP filtered analytic-signal in Fig. 11a, the log-Gabor filtered analytic-signal shows a steadier instantaneous frequency around the fundamental ply-resonance frequency in Fig. 11b. The ME^i and the $STDE^i$ obtained from the 5 MHz signals are compared in Fig.12.

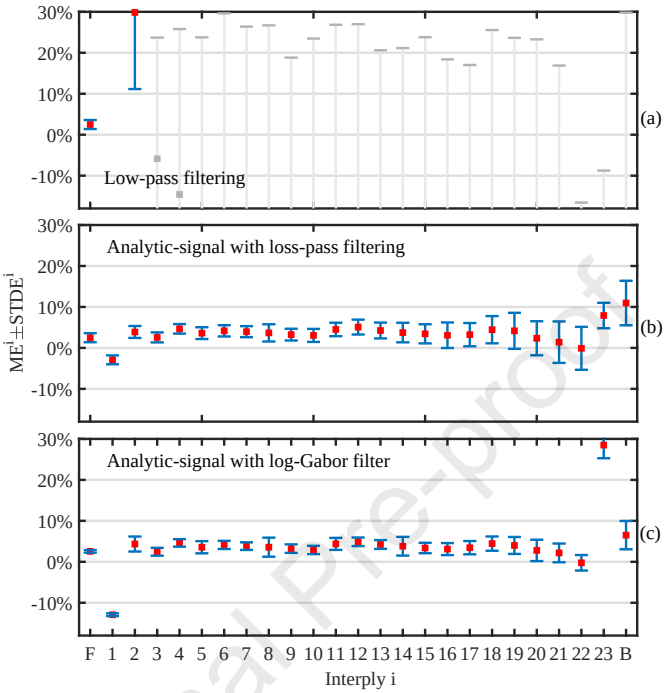

Figure 12: Error bars representing the ME^i and the $STDE^i$ of the estimated interplies from (a) the instantaneous amplitude of the 5 MHz LP filtered signal, and the instantaneous phase of the 5 MHz (b) LP filtered and (c) log-Gabor filtered signals. The data is represented as $ME^i \pm STDE^i$.

While the instantaneous amplitude does not give any indication of the positions of the interplies, the instantaneous phase provides steady results for all interplies. It is worth noting that the $STDE^i$ is significantly improved by the application of the log-Gabor filter. However, the estimated TOF of the interplies near the surfaces shows large ME^i (around -15% for the 1st interply and +28% for the 23rd interply) due to the dominating effect of the front- and back-wall echoes [44]. Compared to the analytic-signal with LP filtering in Fig. 12b, the log-Gabor filter reduces the random errors considerably, but magnifies the ME^i in the 1st and the last plies. The $STDE^i$ steadily increases with depth, but remains below 5% by application of the log-Gabor filter, indicating the high robustness of the TOF estimation. The log-Gabor filter is suggested as a better choice because of its high robustness.

3.5. Comparative analysis for different noise levels

The performance of the various techniques for different noise levels is investigated in this section. The results for 3 SNRs (25 dB, 20 dB and 15 dB) are simulated and analyzed. Fig. 13 compares the ME^i and the $STDE^i$ for the various techniques and noise levels.

From Fig. 13, it is clear that the 50 MHz ultrasound coupled to the LP filtering is not a good approach for extracting the deep interply locations. For the SNR of 15 dB, this method already yields random results from the 7th interply on. On the other hand, it keeps a very high resolution and good stability for the near-surface plies under all the considered noise levels. In a similar way, the 15 MHz ultrasound with Wiener deconvolution becomes more unstable for lower SNR. The $STDE^i$ increase significantly with the SNR, and for the lowest SNR of 15 dB the performance of this approach dropped significantly.

In contrast to previous techniques, the 5 MHz ultrasound coupled to analytic-signal analysis with log-Gabor filter performs very well for all considered noise levels. Further, for the SNR of 25 dB and 20 dB it can be noted that the ME^i

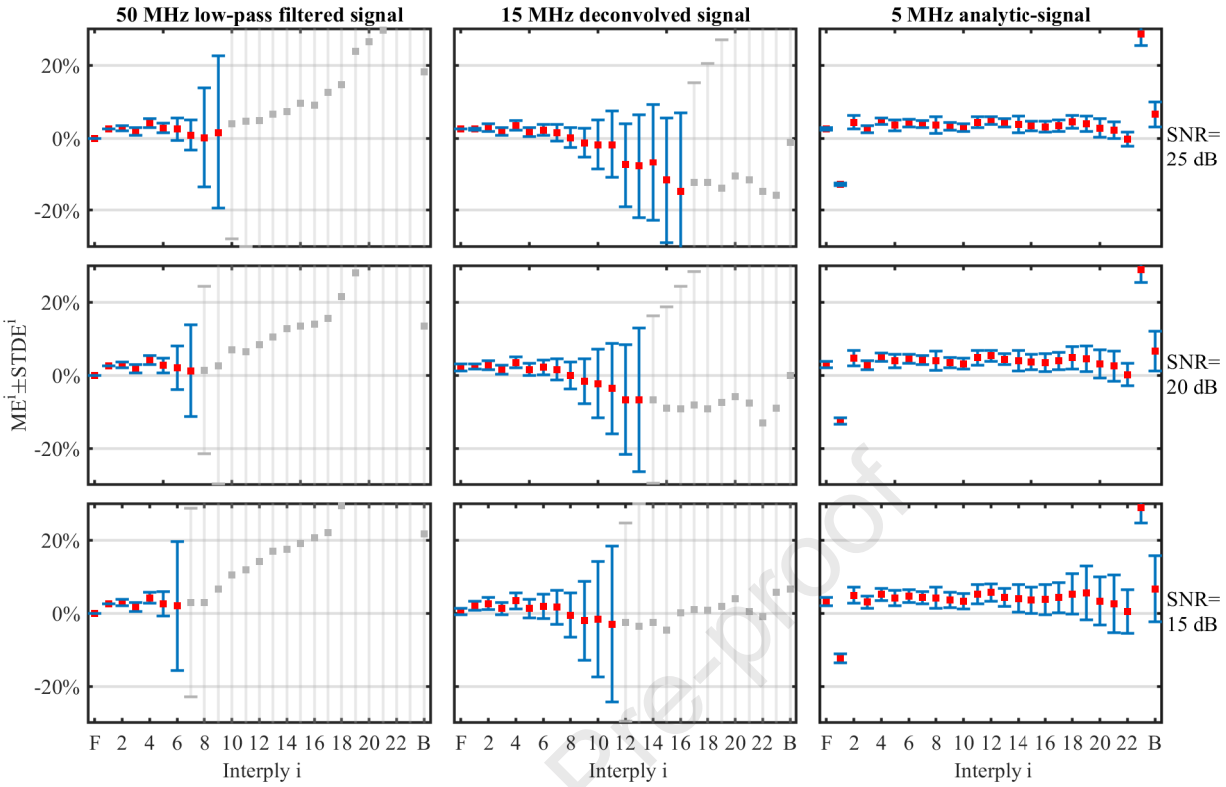

Figure 13: Error bars representing the ME^i and the $STDE^i$ of the estimated interplies from the 50 MHz LP filtered signal (first column), the 15 MHz signal with Wiener deconvolution (second column), and the 5 MHz analytic-signal with log-Gabor filter (third column). Results are obtained for different SNRs: 25 dB (first row), 20 dB (second row), and 15 dB (third row). The data is represented as $ME^i \pm STDE^i$.

of the second and second last interply peaks, while their $STDE^i$ is very small. This indicates a systematic error in the extraction of the location of these two interplies through the instantaneous phase [44, 47]. For the lowest SNR, the ME^i remains quite stable over all interplies, although the $STDE^i$ increases to some extent. The good performance for all considered SNR levels can be attributed to the use of a log-Gabor filter. Indeed, apart from providing an appropriate scale selection, it also suppresses noise features.

4. Experimental study

4.1. Materials and Methods

A CFRP laminate (autoclave manufactured) with dimension 150 mm Œ 100 mm and a thickness of 5.52 mm is studied. It consists of 24 unidirectional plies and has a stacking sequence $[45/0/-45/90]_{3s}$. Each ply is assumed to have a constant and uniform thickness. The inspection procedure takes approximately 10 minutes, such that water diffusion in the inspected composite sample is of little concern [64, 65].

Three different spherically focused broadband immersion transducers (center frequency of 5 MHz, 15 MHz, and 50 MHz) are employed. Table 4 presents the properties of the transducers applied in this experimental study. Reference signals reflected from a thick steel plate are acquired to calculate the SNR and the bandwidth (at -6 dB) of different transducers. The reference signal of the 15 MHz transducer is used as the deconvolution kernel for the Wiener deconvolution. The transducers are excited by an ultrasonic pulser (Tecscan UTPR-CC-50). The exciting pulse is a negative square wave with a pulse width of 30-500 ns (according to the setting), a rise time below 5 ns, and a fall time below 20 ns. The employed settings for the pulser including the voltage, capacity, and damping are also presented in Table 4. To achieve the raster scanning, a 3-axis Cartesian scanner is used which is controlled using a motion controller card (NI PXI-7350). The scanning steps in both x and y directions are 0.5 mm and the scanning area X×Y = 50 mm×50

Table 4
The properties of the employed transducers and the corresponding settings for the pulser

Properties of transducers							Settings for pulser		
Manufacturer	Code	Freq.	Bandwidth (-6 dB)	Elem. d.	Focal l.	SNR	Voltage	Capacity	Damping
GE	H5M	5 MHz	2.43 - 6.61 MHz	6.35 mm	25.4 mm	39.42 dB	120 V	1070 pF	45 Ohm
Olympus	V313	15 MHz	10.84 - 23.08 MHz	6.35 mm	25.4 mm	28.20 dB	120 V	920 pF	78 Ohm
Olympus	V390	50 MHz	26.31 - 61.85 MHz	6.35 mm	12.7 mm	26.84 dB	120 V	450 pF	500 Ohm

mm (100×100 data points) for all transducers. The scanning procedure and excitation/acquisition sequence have been programmed in a custom-made LabVIEW® program. The reflected signals from the CFRP laminate, for the different employed transducers, are displayed in A-scan mode in Fig. 14.

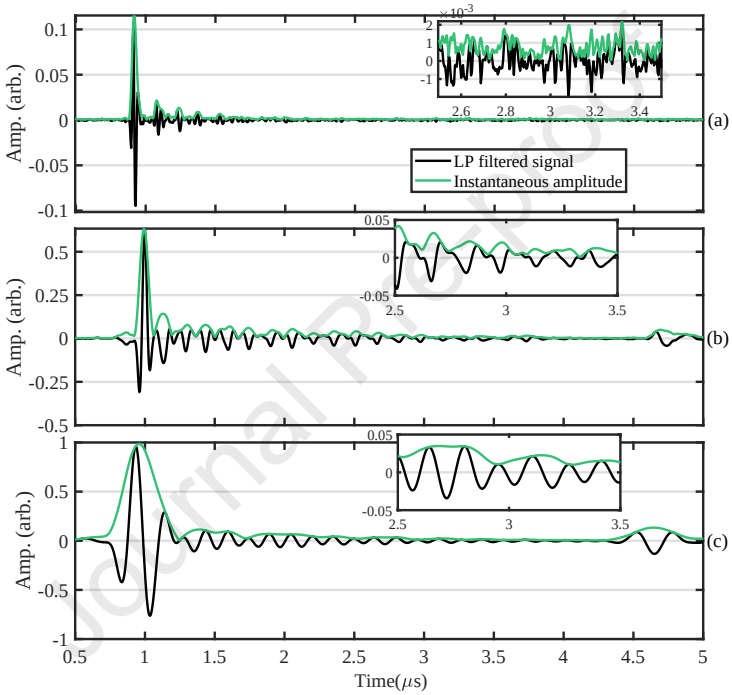

Figure 14: The LP filtered signal, including the instantaneous amplitude (green trace), from the CFRP laminate for different employed transducers with center frequency (a) 50 MHz, (b) 15 MHz, and (c) 5 MHz.

After collecting the data by the raster scanning, the 3D data matrix is sent to Matlab® in order to reconstruct the positions of the interplies using the flow chart presented in section 3.3. According to the instantaneous amplitude of the 5 MHz LP filtered signals, the TOF between the front- and back-wall echo is approximately 3.67 μs, which indicates an approximate ply-resonance frequency of 6.5 MHz. Thus, the center frequency and σ_0 of the log-Gabor filter applied on the 5 MHz signals are chosen as 6.5 MHz and 0.7 respectively.

4.2. Comparison and discussion

Fig. 15 displays the B-scan representation at Y = 25 mm of the instantaneous amplitude from the 50 MHz LP filtered signals, the 15 MHz Wiener deconvolved signals, and the 5 MHz log-Gabor filtered signals. 3 optimal techniques are here applied to estimate positions of the interplies as follows:

Method 1: the 50 MHz LP filtered signal using analysis of the instantaneous amplitude,
Method 2: the 15 MHz Wiener deconvolved signal using analysis of the instantaneous amplitude,
Method 3: the 5 MHz log-Gabor filtered analytic-signal using analysis of the instantaneous phase.

The estimated positions of the interplies and the uniformed-spaced positions of the interplies are superimposed on these B-scan images. The difference in the quality to extract the interply locations can be readily seen in Fig. 15. In order to quantify this, the thicknesses of the plies are estimated from the estimated positions of the interplies in each data point. The mean estimated thickness MT^p and the standard deviations of the estimated thickness $STDT^p$ of the pth ply are calculated as:

$$MT^p = \frac{\sum_{q=1}^{m} T_q^p}{m}, \tag{27}$$

$$STDT^p = \sqrt{\frac{\sum_{q=1}^{m} (T_q^p - \overline{T_q^p})^2}{m}}, \tag{28}$$

where T_q^p is the estimated thickness of the pth ply from the A-scan in the qth data point, and m is the number of the data points in the scanning area (100×100=10000).

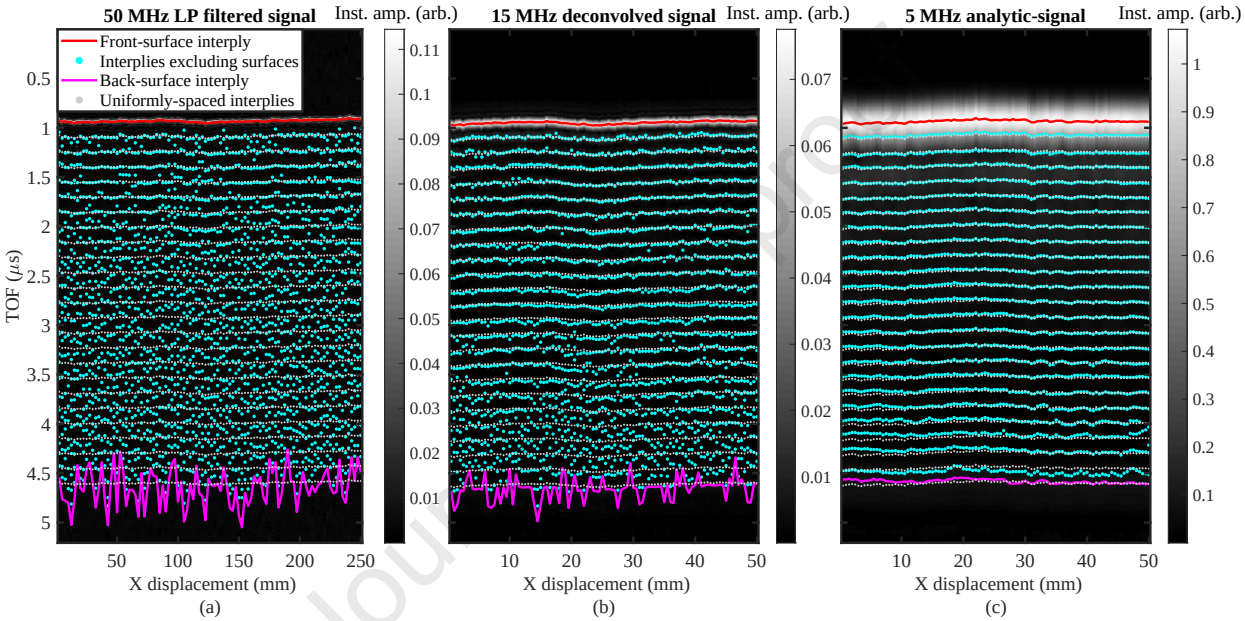

Figure 15: B-scan ultrasound images (at Y = 25 mm) of the instantaneous amplitude from (a) 50 MHz LP filtered signals, (b) 15 MHz signals with Wiener deconvolution, and (c) 5 MHz analytic-signals with log-Gabor filter. Superimposed are the estimated positions of the interplies and the uniformly-spaced positions of the interplies

Note that care has to be taken when interpreting these metrics because they include the variation of the actual thickness in each single ply. Fig. 16 displays the obtained MT^p and $STDT^p$ for the three considered cases. From the total thickness of the sample (5.52 mm), and the true number of plies (24 plies), the expected thickness of a single ply is calculated as 5.52/24 = 0.23 mm (see the dashed line in Fig. 16). This is of course under the assumption that the autoclave manufacturing process yields a uniformly-spaced ply thickness (T^{us}) over depth and over the CFRP sample. Similarly as for the numerical case, if the $STDT^p$ becomes higher than 22% the T^{us}, the extracted results are assumed to be random and are therefore greyed out in the graph.

The 50 MHz signals show a very uniform MT^p over the full depth (see Fig. 16a). However, evaluation of $STDT^p$ tells a different story and indicates the randomness of the estimated ply thickness for deeper plies. This can be also verified in Fig. 15a. Hence, this clearly indicates the poor performance and robustness of this method to resolve the ply structure of the CFRP composite. The 15 MHz signals with Wiener deconvolution provide better probing depth and robustness (see Fig. 15b). Nearly 18 plies can be distinguished, but the $STDT^p$ increases significantly with depth. This can also be verified in Fig. 16b.

The 5 MHz analytic-signals with log-Gabor filter provide the best results and are able to extract all 24 plies in a stable and robust way (see Fig. 16c). This can be also verified in Fig. 15c. However, one of the issues that emerge from these results is that there are large systematic errors in the most shallow and deepest plies. The estimated thicknesses of

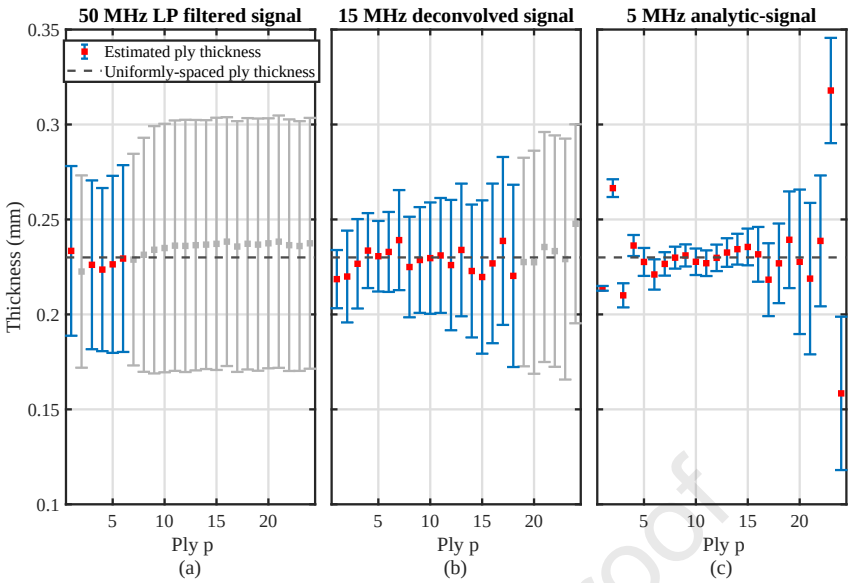

Figure 16: Error bars representing the MT^p and the $STDT^p$ of the plies from (a) 50 MHz LP filtered signals, (b) 15 MHz signals with Wiener deconvolution, and (c) 5 MHz analytic-signals with log-Gabor filter. The data is represented as $MT^p \pm STDT^p$.

those plies show significant deviations from the T^{us} (see Fig. 16c). A similar observation was made in the simulation study (see Fig. 12c), and this systematic deviation has been attributed to the dominating effect of the front- and back-wall echo.

Fig. 17 provides a C-scan representation of the estimated depth of several interplies by considering the three afore-

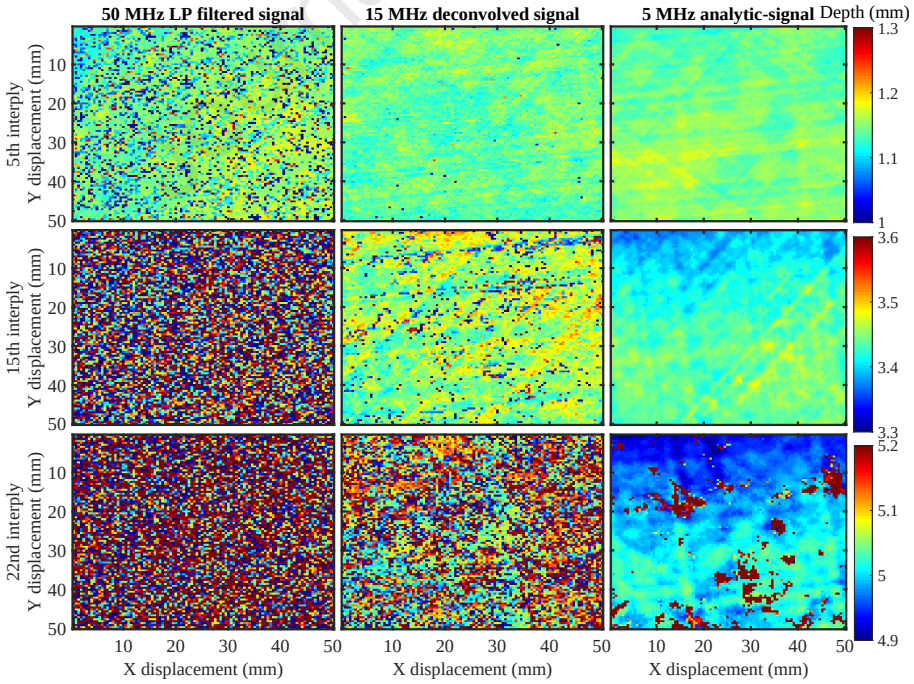

Figure 17: The profiles of the 5th (first row), the 15th (second row), and the 22nd (third row) estimated interplies respectively. The interplies are estimated from the 50 MHz LP filtered signals (first column), the 15 MHz deconvolved signals (second column), and the 5 MHz analytic-signals (third column) respectively.

mentioned techniques. The images of the depth profiles reconstructed by the 50 MHz LP filtered signals are evidently very noisy. One could say that the profile of the 5th interply can be extracted, though with low quality. The 15 MHz signals with Wiener deconvolution can reconstruct the profiles of the 5th and 15th interplies with higher quality but yield fully unstable results for the 22nd ply. The 5 MHz analytic-signals with log-Gabor filter successfully reconstruct the depth profile of all the interplies with high quality. Although, it is clear that the depth profile of the 22nd interply becomes more unsteady and less accurate.

It is important to note that there is an intrinsic difference in the noise level between the different transducers (see Table 4). The higher frequency transducer intrinsically produces more noise due to the electrical power loss as well as the mechanical power loss [66]. Therefore, the low-frequency signals tend to be naturally more stable than the high-frequency signals. This also contributes to worse performance of the 50 MHz and the 15 MHz signals in the experiments. Another potential problem of using high-frequency ultrasound is that it could be sensitive to fiber tows inside the plies [67]. There is an obvious difficulty in reconstructing the positions of the interplies because the echoes from the fiber tows could be mistaken as the echoes from the interplies.

5. Conclusions

This study discussed and compared several ultrasonic techniques, operating in different frequency ranges, for reconstructing the multilayered structure of composites. The performance of the different ultrasonic techniques is investigated on synthetic ultrasonic data, with various noise levels, a representative for a 24 layer composite immersed in water. It is revealed that the 50 MHz ultrasound with LP filtering, coupled to the analysis of the instantaneous amplitude, can only effectively distinguish the near-surface interplies with good robustness. The 15 MHz ultrasound has better probing depth and yields reasonably stable estimation, especially when it is coupled to Wiener deconvolution. Though, for the deeper interplies the results become unstable and their locations could not be extracted in a robust manner. Finally, the 5 MHz ultrasound coupled to analytic-signal analysis provides the best robustness and probing depth under all noise levels. This approach makes use of the ply-resonance (around 6.5 MHz for the here considered multilayered structure), and evaluates the instantaneous phase in order to estimate the depth of the interplies. This approach yields good results over the full depth of the considered multilayered structure, especially when coupled to a log-Gabor filter for optimal scaling of the signals. However, the analytic-signal results also indicate a systematic deviation in the depth estimation of the two interplies closest to the front- and back surface. This is attributed to the dominating effect of the front- and back-wall echo which locally distorts the instantaneous phase profile.

Also, an experimental study on a $[45/0/-45/90]_{3s}$ CFRP sample with 24 plies is reported. The CFRP sample has been raster-scanned in pulse-echo mode with several transducers operating in different frequency ranges. The estimated interply locations are displayed in B-scan mode, and the extracted ply thicknesses are compared with the nominal ply thickness. The profiles of the estimated interplies at several depths are displayed in C-scan mode. The obtained experimental results fully confirm the observations and results from the simulation study.

The comparative analysis of this research provides deeper insights into the performance of the ultrasonic techniques operating in different frequency ranges. It could serve as a base for selecting the appropriate ultrasonic techniques for reconstructing the multilayered structure of composite laminates.

6. Acknowledgment

This work is supported by China Scholarship Council and Ghent University Preference CSC program (No. 01SC0219), Bijzonder OnderzoeksFonds Ghent University (BOF 01N01719), ALMA project (HBC.2018.0427) which fits in the research program STREAM funded by SIM (Strategic Initiative Materials in Flanders) and VLAIO (Flemish government agency Innovation & Entrepreneurship), and the National Natural Science Foundation of China (No. U1709206).

References

[1] Karataş, M.A., Gökkaya, H.. A review on machinability of carbon fiber reinforced polymer (cfrp) and glass fiber reinforced polymer (gfrp) composite materials. Def Technol 2018;14(4):318–326. doi:https://doi.org/10.1016/j.dt.2018.02.001.

[2] Rajak, D.K., Pagar, D.D., Menezes, P.L., Linul, E.. Fiber-reinforced polymer composites: Manufacturing, properties, and applications. Polymers 2019;11(10):1667. doi:https://doi.org/10.3390/polym11101667.

[3] Amafabia, D.M., Montalvão, D., David-West, O., Haritos, G.. A review of structural health monitoring techniques as applied to composite structures. SDHM 2018;11(2):91–147. doi:https://doi.org/10.3970/sdhm.2017.011.091.

[4] Linul, E., Vălean, C., Linul, P.A.. Compressive behavior of aluminum microfibers reinforced semi-rigid polyurethane foams. Polymers 2018;10(12):1298. doi:https://doi.org/10.3390/polym10121298.
[5] Chukov, D., Nematulloev, S., Torokhov, V., Stepashkin, A., Sherif, G., Tcherdyntsev, V.. Effect of carbon fiber surface modification on their interfacial interaction with polysulfone. Results Phys 2019;15:102634. doi:https://doi.org/10.1016/j.rinp.2019.102634.
[6] Wang, B., Zhong, S., Lee, T.L., Fancey, K.S., Mi, J.. Non-destructive testing and evaluation of composite materials/structures: A state-of-the-art review. Adv Mech Eng 2020;12(4):1687814020913761. doi:https://doi.org/10.1177/1687814020913761.
[7] Gholizadeh, S.. A review of non-destructive testing methods of composite materials. Procedia Structural integr 2016;1:50–57. doi:https://doi.org/10.1016/j.prostr.2016.02.008.
[8] Duchene, P., Chaki, S., Ayadi, A., Krawczak, P.. A review of non-destructive techniques used for mechanical damage assessment in polymer composites. J Mater Sci 2018;53(11):7915–7938. doi:https://doi.org/10.1007/s10853-018-2045-6.
[9] Emerson, M.J., Jespersen, K.M., Dahl, A.B., Conradsen, K., Mikkelsen, L.P.. Individual fibre segmentation from 3d x-ray computed tomography for characterising the fibre orientation in unidirectional composite materials. Compos Part A Appl Sci Manuf 2017;97:83–92. doi:https://doi.org/10.1016/j.compositesa.2016.12.028.
[10] Park, D.W., Oh, G.H., Kim, D.J., Kim, H.S.. In-situ thickness measurement of epoxy molding compound in semiconductor package products using a terahertz-time of flight system. NDT E Int 2019;105:11–18. doi:https://doi.org/10.1016/j.ndteint.2019.04.012.
[11] Park, D.W., Oh, G.H., Kim, H.S.. Predicting the stacking sequence of e-glass fiber reinforced polymer (gfrp) epoxy composite using terahertz time-domain spectroscopy (thz-tds) system. Compos B Eng 2019;177:107385. doi:https://doi.org/10.1016/j.compositesb.2019.107385.
[12] Meola, C., Carlomagno, G.M.. Infrared thermography to evaluate impact damage in glass/epoxy with manufacturing defects. Int J Impact Eng 2014;67:1–11. doi:https://doi.org/10.1016/j.ijimpeng.2013.12.010.
[13] Poelman, G., Hedayatrasa, S., Segers, J., Van Paepegem, W., Kersemans, M.. Adaptive spectral band integration in flash thermography: Enhanced defect detectability and quantification in composites. Compos B Eng 2020;202:108305. doi:https://doi.org/10.1016/j.compositesb.2020.108305.
[14] De Angelis, G., Meo, M., Almond, D.P., Pickering, S.G., Angioni, S.L.. A new technique to detect defect size and depth in composite structures using digital shearography and unconstrained optimization. NDT E Int 2012;45(1):91–96. doi:https://doi.org/10.1016/j.ndteint.2011.07.007.
[15] Mizukami, K., Mizutani, Y., Kimura, K., Sato, A., Todoroki, A., Suzuki, Y.. Detection of in-plane fiber waviness in cross-ply cfrp laminates using layer selectable eddy current method. Compos Part A Appl Sci Manuf 2016;82:108–118. doi:https://doi.org/10.1016/j.compositesa.2015.11.040.
[16] Mizukami, K., Mizutani, Y., Todoroki, A., Suzuki, Y.. Detection of in-plane and out-of-plane fiber waviness in unidirectional carbon fiber reinforced composites using eddy current testing. Compos B Eng 2016;86:84–94. doi:https://doi.org/10.1016/j.compositesb.2015.09.041.
[17] Harizi, W., Chaki, S., Bourse, G., Ourak, M.. Mechanical damage characterization of glass fiber-reinforced polymer laminates by ultrasonic maps. Compos B Eng 2015;70:131–137. doi:https://doi.org/10.1016/j.compositesb.2014.11.014.
[18] Kersemans, M., Martens, A., Lammens, N., Van Den Abeele, K., Degrieck, J., Zastavnik, F., et al. Identification of the elastic properties of isotropic and orthotropic thin-plate materials with the pulsed ultrasonic polar scan. Exp Mech 2014;54(6):1121–1132. doi:https://doi.org/10.1007/s11340-014-9861-7.
[19] Song, H., Yang, Y.. Super-resolution visualization of subwavelength defects via deep learning-enhanced ultrasonic beamforming: A proof-of-principle study. NDT E Int 2020;116:102344. doi:https://doi.org/10.1016/j.ndteint.2020.102344.
[20] Shoukroun, D., Massimi, L., Iacoviello, F., Endrizzi, M., Bate, D., Olivo, A., et al. Enhanced composite plate impact damage detection and characterisation using x-ray refraction and scattering contrast combined with ultrasonic imaging. Compos B Eng 2020;181:107579. doi:https://doi.org/10.1016/j.compositesb.2019.107579.
[21] Blandford, B.M., Jack, D.A.. High resolution depth and area measurements of low velocity impact damage in carbon fiber laminates via an ultrasonic technique. Compos B Eng 2020;188:107843. doi:https://doi.org/10.1016/j.compositesb.2020.107843.
[22] Caminero, M., García-Moreno, I., Rodríguez, G., Chacón, J.. Internal damage evaluation of composite structures using phased array ultrasonic technique: Impact damage assessment in cfrp and 3d printed reinforced composites. Compos B Eng 2019;165:131–142. doi:https://doi.org/10.1016/j.compositesb.2018.11.091.
[23] Wronkowicz, A., Dragan, K., Lis, K.. Assessment of uncertainty in damage evaluation by ultrasonic testing of composite structures. Compos Struct 2018;203:71–84. doi:https://doi.org/10.1016/j.compstruct.2018.06.109.
[24] Morokov, E., Levin, V., Chernov, A., Shanygin, A.. High resolution ply-by-ply ultrasound imaging of impact damage in thick cfrp laminates by high-frequency acoustic microscopy. Compos Struct 2021;256:113102.
[25] Wang, D., He, X., Xu, Z., Jiao, W., Yang, F., Jiang, L., et al. Study on damage evaluation and machinability of ud-cfrp for the orthogonal cutting operation using scanning acoustic microscopy and the finite element method. Materials 2017;10(2):204. doi:https://doi.org/10.3390/ma10020204.
[26] Bai, X., Sun, Z., Sun, A., Chen, J., Ju, B.F.. Determination of the multiple local properties of thin layer with high lateral resolution by scanning acoustic microscopy. Rev Sci Instrum 2014;85(9):094901. doi:https://doi.org/10.1063/1.4894261.
[27] Ono, K.. A comprehensive report on ultrasonic attenuation of engineering materials, including metals, ceramics, polymers, fiber-reinforced composites, wood, and rocks. Appl Sci 2020;10(7):2230. doi:https://doi.org/10.3390/app10072230.
[28] Mohammadkhani, R., Zanotti Fragonara, L., Padiyar M, J., Petrunin, I., Raposo, J., Tsourdos, A., et al. Improving depth resolution of ultrasonic phased array imaging to inspect aerospace composite structures. Sensors 2020;20(2):559. doi:https://doi.org/10.3390/s20020559.
[29] Abdessalem, B., Ahmed, K., Redouane, D.. Signal quality improvement using a new tmsse algorithm: Application in delamination detection in composite materials. J Nondestr Eval 2017;36(1):16. doi:https://doi.org/10.1007/s10921-017-0398-4.

[30] Burrows, S.E., Fan, Y., Dixon, S.. High temperature thickness measurements of stainless steel and low carbon steel using electromagnetic acoustic transducers. NDT E Int 2014;68:73–77. doi:https://doi.org/10.1016/j.ndteint.2014.07.009.
[31] Losada, R.A.. Practical fir filter design in matlab. The Math Works inc Revision 2004;1:5–26.
[32] Sin, S.K., Chen, C.H.. A comparison of deconvolution techniques for the ultrasonic nondestructive evaluation of materials. IEEE Trans Image Process 1992;1(1):3–10. doi:https://doi.org/10.1109/83.128026.
[33] Neal, S.P., Speckman, P.L., Enright, M.. Flaw signature estimation in ultrasonic nondestructive evaluation using the wiener filter with limited prior information. IEEE Trans Ultrason Ferroelectr Freq Control 1993;40(4):347–353. doi:https://doi.org/10.1109/58.251283.
[34] Miyashita, T., Schwetlick, H., Kessel, W.. Recovery of ultrasonic impulse response by spectral extrapolation. In: Acoustical Imaging. Springer; 1985, p. 247–257. doi:https://doi.org/10.1007/978-1-4613-2523-9_23.
[35] Zala, C., Barrodale, I., McRae, K.. High resolution deconvolution of ultrasonic traces. In: Signal processing and pattern recognition in nondestructive evaluation of materials. Springer; 1988, p. 101–108. doi:https://doi.org/10.1007/978-3-642-83422-6_7.
[36] Honarvar, F., Sheikhzadeh, H., Moles, M., Sinclair, A.N.. Improving the time-resolution and signal-to-noise ratio of ultrasonic nde signals. Ultrasonics 2004;41(9):755–763. doi:https://doi.org/10.1016/j.ultras.2003.09.004.
[37] Karslı, H.. Further improvement of temporal resolution of seismic data by autoregressive (ar) spectral extrapolation. J Appl Geophy 2006;59(4):324–336. doi:https://doi.org/10.1016/j.jappgeo.2005.11.001.
[38] Wei, L., Huang, Z.y., Que, P.w.. Sparse deconvolution method for improving the time-resolution of ultrasonic nde signals. NDT E Int 2009;42(5):430–434. doi:https://doi.org/10.1016/j.ndteint.2009.01.009.
[39] Wiggins, R.A.. Minimum entropy deconvolution. Geoexploration 1978;16(1-2):21–35. doi:https://doi.org/10.1016/0016-7142(78)90005-4.
[40] Lee, J.Y., Nandi, A.. Extraction of impacting signals using blind deconvolution. J Sound Vib 2000;232(5):945–962. doi:https://doi.org/10.1006/jsvi.1999.2778.
[41] Nandi, A.K., Mampel, D., Roscher, B.. Blind deconvolution of ultrasonic signals in nondestructive testing applications. IEEE Trans Signal Process 1997;45(5):1382–1390. doi:https://doi.org/10.1109/78.575716.
[42] Boßmann, F., Plonka, G., Peter, T., Nemitz, O., Schmitte, T.. Sparse deconvolution methods for ultrasonic ndt. J Nondestr Eval 2012;31(3):225–244. doi:https://doi.org/10.1007/s10921-012-0138-8.
[43] Chang, Y., Zi, Y., Zhao, J., Yang, Z., He, W., Sun, H.. An adaptive sparse deconvolution method for distinguishing the overlapping echoes of ultrasonic guided waves for pipeline crack inspection. Meas Sci Technol 2017;28(3):035002. doi:http://dx.doi.org/10.1088/1361-6501/aa52ae.
[44] Smith, R.A., Nelson, L.J., Mienczakowski, M.J., Wilcox, P.D.. Ultrasonic analytic-signal responses from polymer-matrix composite laminates. IEEE Trans Ultrason Ferroelectr Freq Control 2017;65(2):231–243. doi:https://doi.org/10.1109/TUFFC.2017.2774776.
[45] Nelson, L., Smith, R., Mienczakowski, M.. Ply-orientation measurements in composites using structure-tensor analysis of volumetric ultrasonic data. Compos Part A Appl Sci Manuf 2018;104:108–119. doi:https://doi.org/10.1016/j.compositesa.2017.10.027.
[46] Nelson, L., Smith, R.. Fibre direction and stacking sequence measurement in carbon fibre composites using radon transforms of ultrasonic data. Compos Part A Appl Sci Manuf 2019;118:1–8. doi:https://doi.org/10.1016/j.compositesa.2018.12.009.
[47] Yang, X., Verboven, E., Ju, B.f., Kersemans, M.. Parametric study on interply tracking in multilayer composites by analytic-signal technology. Ultrasonics 2021;111:106315. doi:https://doi.org/10.1016/j.ultras.2020.106315.
[48] Smith, R.A., Nelson, L.J., Mienczakowski, M.J., Wilcox, P.D.. Ultrasonic tracking of ply drops in composite laminates. In: AIP Conference Proceedings; vol. 1706. AIP Publishing LLC; 2016, p. 050006.
[49] Neal, S.P., Thompson, D.O.. A prior knowledge based optimal wiener filtering approach to ultrasonic scattering amplitude estimation. J Acoust Soc Am 1989;86(S1):S94–S94. doi:https://doi.org/10.1121/1.2027743.
[50] Ulrych, T.J., Bishop, T.N.. Maximum entropy spectral analysis and autoregressive decomposition. Rev Geophys 1975;13(1):183–200. doi:https://doi.org/10.1029/RG013i001p00183.
[51] Shakibi, B.. Resolution enhancement of ultrasonic signals using autoregressive spectral extrapolation. Ph.D. thesis; 2011.
[52] Bridge, C.P.. Introduction to the monogenic signal. 2017. arXiv:1703.09199.
[53] Field, D.J.. Relations between the statistics of natural images and the response properties of cortical cells. J Opt Soc Am A 1987;4(12):2379–2394. doi:https://doi.org/10.1364/JOSAA.4.002379.
[54] Boukerroui, D., Noble, J.A., Brady, M.. On the choice of band-pass quadrature filters. J Math Imaging Vis 2004;21(1-2):53–80. doi:https://doi.org/10.1023/B:JMIV.0000026557.50965.09.
[55] Brekhovskikh, L.M.. Waves in layered media. New York: Academic Press; 1960, p. 22–26.
[56] Cann, M.T., Adams, D.O., Schneider, C.L.. Characterization of fiber volume fraction gradients in composite laminates. J Compos Mater 2008;42(5):447–466. doi:https://doi.org/10.1177/0021998307086206.
[57] Hallal, A., Younes, R., Fardoun, F., Nehme, S.. Improved analytical model to predict the effective elastic properties of 2.5 d interlock woven fabrics composite. Compos Struct 2012;94(10):3009–3028. doi:https://doi.org/10.1016/j.compstruct.2012.03.019.
[58] Sevenois, R., Garoz, D., Verboven, E., Spronk, S., Gilabert, F., Kersemans, M., et al. Multiscale approach for identification of transverse isotropic carbon fibre properties and prediction of woven elastic properties using ultrasonic identification. Compos Sci Technol 2018;168:160–169. doi:https://doi.org/10.1016/j.compscitech.2018.09.016.
[59] Davila, Y., Crouzeix, L., Douchin, B., Collombet, F., Grunevald, Y.H.. Spatial evolution of the thickness variations over a cfrp laminated structure. Appl Compos Mater 2017;24(5):1201–1215. doi:https://doi.org/10.1007/s10443-016-9573-5.
[60] Collombet, F., Mulle, M., Grunevald, Y.H., Zitoune, R.. Contribution of embedded optical fiber with bragg grating in composite structures for tests-simulations dialogue. Mech Adv Mater Struct 2006;13(5):429–439. doi:https://doi.org/10.1080/15376490600777616.
[61] Smith, R.A.. Use of 3d ultrasound data sets to map the localised properties of fibre-reinforced composites. Ph.D. thesis; University of Nottingham; 2010.
[62] Jeong, H., Hsu, D.K.. Experimental analysis of porosity-induced ultrasonic attenuation and velocity change in carbon composites. Ultrasonics

1995;33(3):195–203. doi:https://doi.org/10.1016/0041-624X(95)00023-V.

[63] Shakibi, B., Honarvar, F., Moles, M., Caldwell, J., Sinclair, A.N.. Resolution enhancement of ultrasonic defect signals for crack sizing. NDT E Int 2012;52:37–50. doi:https://doi.org/10.1016/j.ndteint.2012.08.003.

[64] Joliff, Y., Bélec, L., Heman, M., Chailan, J.F.. Experimental, analytical and numerical study of water diffusion in unidirectional composite materials–interphase impact. Comput Mater Sci 2012;64:141–145. doi:https://doi.org/10.1016/j.commatsci.2012.05.029.

[65] Peret, T., Clement, A., Freour, S., Jacquemin, F.. Homogenization of fickian and non-fickian water diffusion in composites reinforced by hydrophobic long fibers: Application to the determination of transverse diffusivity. Compos Struct 2019;226:111191. doi:https://doi.org/10.1016/j.compstruct.2019.111191.

[66] Karafi, M.R., Khorasani, F.. Evaluation of mechanical and electric power losses in a typical piezoelectric ultrasonic transducer. Sens Actuators A Phys 2019;288:156–164. doi:https://doi.org/10.1016/j.sna.2018.12.044.

[67] Moon, M., Yun, Y., Yoo, M., Song, J., Oh, J.. Carbon fiber manufacturing and applications as a benchmark for nanotube superfiber development. In: Nanotube Superfiber mater. Elsevier; 2019, p. 879–896. doi:https://doi.org/10.1016/B978-0-12-812667-7.00034-3.

Declaration of interests

☒ The authors declare that they have no known competing financial interests or personal relationships that could have appeared to influence the work reported in this paper.

☐The authors declare the following financial interests/personal relationships which may be considered as potential competing interests: